This paper is a non-peer reviewed preprint submitted to Remote Sensing of Environment. The published journal article derived from this preprint has this DOI: 10.1016/j.rse.2022.113294

From Satellite Interferometry displacements to potential damage maps: a tool for risk reduction and urban planning

Anna Barra[a], Cristina Reyes-Carmona[b], Gerardo Herrera[b], Jorge Pedro Galve[c], Lorenzo Solari[a], Rosa María Mateos[b], Jose Miguel Azañón[c], Marta Béjar-Pizarro[b], Juan López-Vinielles[b], Riccardo Palamà[a], Michele Crosetto[a], Roberto Sarro[b], José Cuervas-Mons[d], Oriol Monserrat[a]

[a] Geomatics Research Unit, Remote Sensing group, Centre Tecnològic Telecomunicacions Catalunya (CTTC/CERCA), Av. Carl Friedrich Gauss, 7, 08860, Castelldefels, Spain (abarra@cttc.cat, lsolari@cttc.cat, rpalama@cttc.cat, mcrosetto@cttc.cat, omonserrat@cttc.cat)

[b] Geohazards InSAR Laboratory and Modelling Group (InSARlab), Geohazards and Climate Change Department, Geological and Mining Institute of Spain from the National Research Council (IGME-CSIC), Alenza, 1, 28003, Madrid, Spain (c.reyes@igme.es, g.herrera@igme.es, rm.mateos@igme.es, m.bejar@igme.es, j.lopez@igme.es, r.sarro@igme.es)

[c] Departamento de Geodinámica, Universidad de Granada (UGR), Calle Prof. Vicente Callao, 3, 18011 Granada, Spain (jpgalve@gmail.com, jazanon@ugr.es)

[d] Departamento de Geología, University of Oviedo, c/ Jesús Arias de Velasco s/n 33005 Oviedo, Spain (jcuervas@geol.uniovi.es)

Abstract

Persistent Scatterer Interferometry (PSI) is a consolidated tool for detecting and monitoring ground surface displacements. The availability of satellite data with free access policy and high monitoring capabilities (in terms of resolution and acquisition frequency) is increasing. Moreover, the first continental displacement map of Europe will be freely available in quarter one 2022 by the latest Copernicus Service, the European Ground Motion services (EGMS). The EGMS will provide ground displacement maps, updated every year, delivering valuable information to a wide range of users, such as public or governmental institutions, industry, academia, and citizens. This vast amount of information needs semi-automatic tools and methodologies to derive user-oriented products that can be easily used by land use and urban planning decision-makers, who are often unfamiliar with PSI. This work proposes a semi-automatic procedure to identify damage prone areas in urban environments from wide-area PSI displacement maps. The proposed method identifies the most significant Active Deformation Areas (ADAs) to calculate three products based on the displacement intensity gradient: the Gradient Intensity Map, the Gradient Vectors and Time Series, and the Potential Damage Map. These products allow identifying buildings and urban structures exposed to potential damage, which could be followed by a more detailed building-based vulnerability and risk assessment. The methodology has been applied to an area of the province of Granada (Andalucía, Spain) but it can be applied to any other urban environment where PSI displacement maps are available. To demonstrate the advantages and limitations of the proposed method, results are discussed in five coastal resorts (Cerro Gordo, Punta de la Mona, Marina del Este, Alfa Mar, and Monte de los Almendros), strongly affected by slope movements. The methodology allowed to derive 175 ADAs from about 200,000 measurement points. About 15 % of the resulting area has been found to correspond to high or very high gradient intensity class, and 192 out of 633 buildings have been identified to be prone to moderate or high potential damage. A damage prediction test has been realised through ROC analysis, based on a damage inventory map derived from field surveys. The results demonstrate the effectiveness of the methodology to localize damaged or potentially damaged buildings, substantially reducing the time of analysis.

1 Introduction

Geological or anthropogenic hazards are one of the main targets for urban planning activities at both local and regional scales. An accurate and updated hazard zoning or susceptibility map is a fundamental tool for urban planning and development (Cascini et al., 2005; Mateos et al., 2020), as it supports decision making in relation to both prevention and mitigation measures. The spatial and temporal characterization of surface movements (e.g., slope instability, landslides, soil settlement or subsidence) and their interaction with urban expansion and human activities, is essential to understand the process at hand and plays a key role in sustainable land use and risk management. The anthropic activity can accelerate natural processes that may have an impact on human lives, and damage or destroy buildings and infrastructures. Damages caused by natural disasters have increased in the last decades due to the growing demographic pressure, urban sprawl, territory mismanagements (Cascini et al., 2005) and the effects of climate change. This increase has had an important impact in terms of economic loss. Remote Sensing (RS) and Earth Observation (EO) techniques allow us to implement a multi-scale and multi-frequency monitoring approach: from small-scale detection and low updating frequency to large scale monitoring and, if necessary, high updating frequency. Among the EO techniques, Advanced Differential Synthetic Aperture Radar Interferometry (A-DInSAR) techniques, and in particular Persistent Scatterer Interferometry (PSI) (Crosetto et al., 2016a), are now considered valuable and reliable tools to provide dense and millimetre-accurate ground motion Measurement Points (MPs) networks over wide areas. In the case of PSI, these MPs are referred to as Persistent Scatterers (PSs). Since the 1990s, the applications of satellite interferometry have been multiple and diversified. Some examples are: geological hazards detection and characterization (Calò et al., 2014; Massonnet et al., 1995, 1993; Massonnet and Feigl, 1998), risk assessment (Solari et al., 2020a, 2018), worksites monitoring (Botey i Bassols et al., 2021), engineering and mining (Krishnakumar et al., 2021; López-Vinielles et al., 2020; Solari et al., 2020b). The new satellite generations are improving their monitoring capability, ensuring regular acquisitions with high temporal frequency and a free-for-all data access. The first mission with these acquisition policies was Copernicus Sentinel-1 (S1), a constellation of

two twin satellites, S1A and S1B, respectively launched in 2014 and 2016. S1 was designed to continue the data flow provided by previous missions (Salvi et al., 2012) and represents a turning point in the use of satellite interferometry. It is a precious resource for systematic long-term,wide-area monitoring. S1 allowed developing the so-called Ground Motion Services (GMSs), i.e. wide-area A-DInSAR-based ground motion monitoring and mapping services. Nowadays, GMSs are emerging and provide displacement maps that are freely accessible at both regional (Confuorto et al., 2021; Montalti et al., 2019; Raspini et al., 2018) and national scales (Dehls et al., 2019; Kalia, 2017; Kalia et al., 2017; Papoutsis et al., 2020). The first continental displacement map of Europe will be provided to users in quarter one 2022 by the latest Copernicus Service, the European Ground Motion services (EGMS) (Costantini et al., 2021; Crosetto et al., 2021, 2020a, 2020b). The EGMS will provide ground displacement maps, updated every year, freely accessible through a visualization and download interface. So far, the EGMS has been implemented as scheduled, so its results will soon be distributed by the European Environment Agency. The direct consequence of the launch of GMSs relates to an increasing accessibility to satellite interferometry data and products, and thus to an increasing interest among a wider range of users, including public or governmental institutions, industry, academia and even the general public. However, interpreting this huge amount of data by using the current analysis tools can be difficult, time-consuming, and poorly effective, especially for non-expert users. In this context, it is necessary to develop semi-automatic tools and methodologies to generate operational and interpreted products. In the last years, the research community and a number of projects (e.g. Safety, U-geohaz, RISKCOAST, MOMIT, etc.) have been focused on the application of post-processing methods to ease the interpretation of PSI products and make them more exploitable for users (Barra et al., 2018, 2017; Bonì et al., 2016; Bovenga et al., 2021; Mirmazloumi et al., 2022; Monserrat et al., 2018; Notti et al., 2014; Raspini et al., 2018).

In this paper, we present a methodology that starts from a S1 PSI displacement map to derive potential damage maps and localize areas where structures and infrastructures are prone to damage. Based on the concept of multi-scale analysis proposed by Cascini et al. (2013), Ferlisi et al. (2019), and Peduto et al.

(2017b, 2017a), our method proposes a two-level approach. First, it starts with a regional-scale detection of the most significant Active Deformation Areas (ADA) (Barra et al., 2017), which support the small-medium scale analysis (less than 1:25,000). Then, it derives, through a local-scale analysis, large-scale information on potential damage for elements (buildings) that are exposed to slow movements, and especially to differential displacements (1:10,000-2,000). The ADA map is the first level of information, which allows the fast identification of potentially unstable areas, which permits in turn the use of further automatic methodologies, such as the approaches developed for the automatic classification of the ADAs (Navarro et al., 2020; Solari et al., 2018), or for the estimation of the potential impact to exposed elements (Pastonchi et al., 2018; Solari et al., 2020a). Here, the ADAs are the starting point to generate a second level of information able to drive deeper analyses, field investigations and prompt intervention. The proposed method is based on landslide intensity values, expressed in terms of spatial gradients of motion, to characterise exposed areas (buildings) and indicate where damage might be expected. The main outputs are (i) the Gradient Intensity map; (ii) the gradient vectors and time series, and (iii) the exposed elements Potential Damage Map. An important aspect of the proposed method is that it is fully based on freely available remote sensing data.

PSI has been widely used to assess the relation between movements and damages due to subsidence (Cigna et al., 2011; Cigna and Tapete, 2021; Ezquerro et al., 2020; Peduto et al., 2017b), uplifts (Drougkas et al., 2020) or landslides (Béjar-Pizarro et al., 2017; Bianchini et al., 2015). Here we illustrate the procedure over a coastal area of around 700 km^2 in the province of Granada (Andalucía, South of Spain), with a focus on some ADAs located on residential slopes, where constructions and infrastructure are suffering severe damages. In those areas, a number of field surveys have been carried out to map the actual damage, with the aim of comparing the field evidence with the outputs of the proposed method. For this purpose, a test analysis based on Receiver Operating Characteristic (ROC) curves has been performed to quantitatively evaluate the prediction capability of our building damage mapping approach. These results have been

119 achieved in the frame of RISKCOAST, a project funded by the Interreg SUDOE program (Ref:
120 SOE3/P4/E0868).

121 After the description of the study area (area of interest, AOI) in Section 2, this document includes a brief
122 introduction to the A-DInSAR (and PSI) techniques (Section 3) to ease the reading for non-experts. Then,
123 the methodology is described in Section 4. Section 5 is focused on the results obtained over the AOI. Finally,
124 the results are discussed (Section 6) and the conclusions are presented (Section 7), summarizing the main
125 strengths and limitations of the method.

126 2 Area of application

127 The proposed methodology is applied over an area of around 705 km^2 (Fig. 1) localized in the districts of
128 Almuñécar and Salobreña, in the province of Granada (Andalucía, South of Spain), which is highly affected
129 by slope movements and subsidence (Chacón et al., 2007; Reyes-Carmona et al., 2021, 2020; Mateos et al.,
130 2017 , Notti et al., 2016). From the late sixties, these districts have undergone strong urban development
131 (Chacón et al., 2019, 2016, 2014), which has often disturbed and reactivated pre-existing coastal landslides
132 (Notti et al., 2015) or even triggered new ones (Chacón et al., 2014). Nowadays, many urban areas and
133 several resorts suffer damages and economic losses due to slope movements. We apply our methodology
134 on five coastal resorts (Fig. 2): Cerro Gordo (1); Punta de la Mona and Marina del Este (2); Alfa Mar (3)
135 and Monte de los Almendros (4). These resorts share a common denominator: they all have been built over
136 steep coastal slopes that are affected by ground instabilities and/or known landslides.

137 In the cases of Cerro Gordo and Marina del Este, both resorts were constructed on pre-existing coastal
138 landslides (Mateos et al. 2017, Notti et al., 2015). The studies conducted at both sites suggest that urban
139 development caused landslide reactivation processes that accelerated during intense rainfall periods. As an
140 example, severe urban damages occurred after a series of heavy rains recorded in winter 2009-2010. The
141 most remarkable case corresponds to the Cerro Gordo resort, which was partially evacuated and declared in
142 state of emergency in 2015 and remains under judicial proceedings today. Monitoring through PSI

techniques confirmed that both landslides (Cerro Gordo and Marina del Este) were active from 2003 to 2009, with velocities ranging from 5 to 15 mm/year. For the cases of Punta de la Mona, Alfa Mar and Monte de los Almendros resorts, there is no information about any pre-existing landslides. Regarding ground movements, Galve et al. (2017) reported, through an InSAR-based analysis, displacement values of up to 8 mm/year from 2003 to 2008 both in Alfa Mar and Monte de los Almendros. In contrast, in the Punta de la Mona resort, no information on ground displacement has been published to date. It should be noted that the papers cited above were the subject of discussion at the Spanish General Council of the Judiciary and the High Commission for Architecture Professionals Conference in 2018. These annual conference addresses issues related to the professional responsibilities and expert assistance of architects in judicial proceedings. In 2018, the InSAR studies developed in the study area were considered by architects and lawyers as very useful tools to provide evidence in judicial proceedings related to buildings affected by unstable ground.

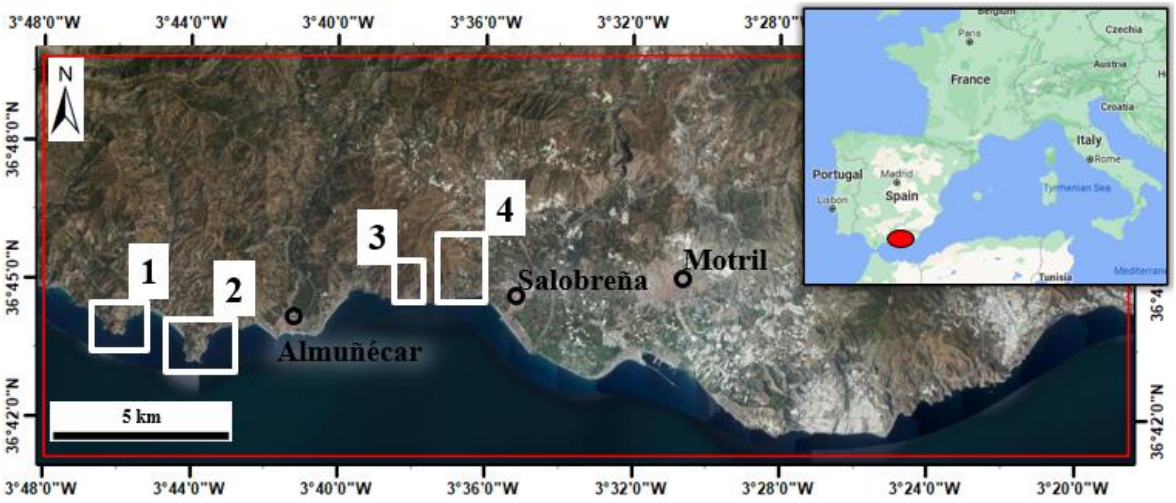

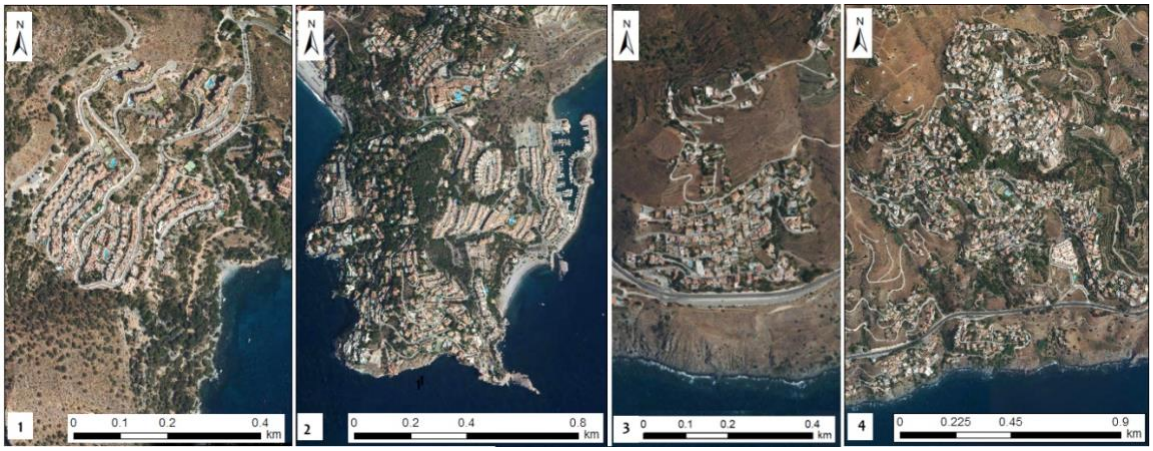

Figure 1: The upper figure shows the coastal western fringe of Granada where the four selected areas are located (1, 2, 3 and 4). The square 1 bounds the Cerro Gordo resort, which is shown in frame 1. The square 2 contains the Punta de la Mona Promontory with two resorts, Punta de la Mona (western side of the promontory) and Marina del Este (eastern side of the promontory), in frame 2. Finaly, the square 3 contains the resort of Alfa Mar, in frame 3, the square 4 contains Monte de los Almendros, in frame 4.

From a geological point of view, the rocks of this coastal area belong to the Alpujárride Complex of the Betic Cordillera (Simancas and Campos, 1993). The Alpujárride Complex is formed by a sequence of metamorphic rocks that are, from bottom to top: (1) dark graphite schists, (2) light schists together with quartzites and (3) marbles (Azañón et al., 1994). Both, the dark and light schists are very deformed and altered, which gives them a ductile and soil-like behaviour (Mateos et al., 2017) and thus makes them not very competent rocks. Moreover, the overlying marbles are densely fractured and karstified, which generates numerous unstable blocks of rocks that easily slide over the schists. These characteristics of the rocks contribute to a very unfavourable mechanic situation that commonly leads to slope instability and landslides along this coastal area.

3 General overview of Satellite Interferometry and PSI

The input of the methodology is a PSI displacement map, consisting of a set of measurement points (MPs) distributed over the processed area. Each MP includes information on the mean annual velocity and on the time series of the displacement occurred in the observed period. The displacement values are obtained at each acquisition of the satellite according to its revisit period, i.e. the time interval between two consecutive

image acquisitions over the same area with the same geometry. The satellite passes over the same area in two geometries of acquisitions: the ascending one, when it moves northward and has a side look from west to east, and the descending one, when it moves southward and has a side look from east to west.

DInSAR techniques measure the surface displacement between two or move SAR image acquisitions over the same area with the same geometry. As opposed to an optical system, DInSAR allows measuring regardless of the presence of clouds or absence of day light. Every image includes information on both the amplitude (intensity), which depends on target characteristics (shape, orientation, roughness, electrical properties), and the phase of the backscattered signal. The phase is mainly related to the two-way path of the signal between the satellite and the target (i.e. the antenna-target distance). Therefore, the phase shift between two images acquired in different times allows measuring an eventual change of distance related with the movement of the target. The sign of the phase difference indicates if the target moves towards (positive) or away (negative) from the satellite. The phase difference (interferogram) is not only influenced by surface displacement, but it also includes other components related to: (i) the different atmosphere conditions at each acquisition time; (ii) the difference of the signal path due to the different position of the satellite at each acquisition; (iii) noise related to a change of the surface conditions (Crosetto et al., 2016). Estimating the other components to extract the movement information is not straightforward. If the displacement component is stronger than the others, and we are interested in punctual events, we can use single pairs of images, acquired before and after the movements, to individually analyse the interferograms (Barra et al., 2016; Hanssen, 2001). To detect slower movements and to generate wide-area displacement maps, it is necessary to apply one of the existing Advanced DInSAR (A-DInSAR), such as the PSI technique. These techniques are based on the use of a stack of images to generate a network of interferograms. A review of PSI methods can be found in Crosetto et al. (2016a). The output of PSI processing is a set of spatially distributed measurement points, known as Persistent Scatterers (PSs), each one representing a ground surface area, where the backscattering characteristics remain stable in time (i.e.

198 coherent, see below) (Ferretti et al., 2001). In the following, a brief overview of the main characteristics of
199 DInSAR and PSI techniques is provided.

200 1) **Geometric characteristics**.

201 DInSAR can only measure motion along the Line-Of-Sight (LOS) direction, which is the direction
202 along which the on-board radar sensor transmits and receives the signal. The LOS direction is
203 oblique (i.e. with an angle with respect to the vertical). DInSAR can only measure the LOS
204 component of the real movement. Consequently, the smaller the angle between the direction of the
205 movement and the LOS, the greater the sensitivity of the technique to measure it. The worst case
206 occurs if the movement is totally perpendicular to the LOS. Due to the side look and slant range
207 nature of SAR systems, depending on the relative geometry between the LOS and the local
208 topography, the footprint (ground resolution) of each pixel changes in space; some slopes cannot
209 be measured because they are "compressed" in few pixels (foreshortening effect).

210 2) **Sampling density**. The capability of measurement depends on the surface characteristics and land
211 cover. Generally, we have PSs where the surface backscattering characteristics remain stable in time
212 (high coherence), as for example over anthropic elements and rock outcrops. On the contrary, PS
213 density decreases in vegetated land and in areas with frequent surface changes, such as open pit
214 mines.

215 3) **Phase measurements**. The interferometric phase allows measuring movements with millimetric
216 precision, but it has the drawback of being ambiguous, causing aliasing errors. Resolving the
217 ambiguities is the main task of phase unwrapping. This operation is one of the main sources of
218 errors, which may generate jumps in the time series. This is usually critical when fast movements
219 occur.

220 4) **Horizontal-Vertical components.** The availability of both ascending and descending data can help
221 to mitigate the geometric limitations of SAR: the steeper the slopes over the study area, the greater
222 the need to process both geometries. The use of two geometries is also needed to derive the

horizontal and vertical components of the movement, which eases data interpretation. The horizontal-vertical decomposition depends on the availability of both ascending and descending data in the same sampling cell. This implies (i) a reduction of the spatial resolution and (ii) the loss of information where an area is not covered by PSs from both trajectories.

5) **Slope Projection.** In slope instability studies, the LOS measurements are usually projected onto the maximum slope direction. The main advantage of this approach is that it does not require data acquired both in ascending and descending geometries. Nevertheless, it is based on the strong assumption that the movement is parallel to the slope. Moreover, the result is strictly dependent on the resolution of the used Digital Elevation Model (DEM) and on the PS positioning accuracy over it, which is not always precise.

4 Methodology

This study seeks to generate maps to identify buildings and urban infrastructures exposed to possible damage. Assessing the potential damage suffered by structures requires at least three elements (Tinti et al., 2011): i) the identification and definition of the parameters affecting the structures; ii) the characteristics of the buildings; iii) the correlation between the intensity of the parameters and the damage levels. Let us consider each element below.

Parameters most frequently used to evaluate the damage probability of slow-moving phenomena (such as subsidence, uplift and landslides) include total displacement, differential displacement, spatial gradient of the displacement, tilts or angular distortions, displacement velocity or depth of the sliding surface (Antronico et al., 2015; Boscawen Burland and Wroth, 1975; Ezquerro et al., 2020; Fell et al., 2008; Mansour et al., 2011; Peduto et al., 2017b). A more detailed analysis of damage probability requires other factors such as the orientation of the building with respect to the displacement vectors, its location within the unstable slope (Mavrouli et al., 2014), the subsoil geology (lithology, lateral discontinuities, water presence) or the soil-structure interaction.

Parameters that are key to perform a detailed vulnerability analysis of buildings (Pavić et al., 2019) are: mechanical parameters of the construction materials; the characteristics of bearing and the distribution and inter-relation between structural (pillars, beams, bearing wall) and non-structural (claddings, non-bearing walls) elements; the geometry (e.g. height/width); the typology and depth of foundations; the construction year; the history of the building in terms of past stress cycles; and the maintenance status, reconstructions, or presence of hidden damage (Boscawen Burland and Wroth, 1975; Lancellotta, 2004; Pavić et al., 2019; Peduto et al., 2017b; Polshin and Tokar, 1957; Skempton and Macdonald, 1956). However, collecting all these parameters over wide urban areas would require a long amount of time.

The correlation between the intensity of the displacement and the damage levels depends upon the characteristics of the exposed elements. The most frequent approaches to study this correlation are empirical studies and fragility curvess, which relate the inventoried damage with the measured displacement (e.g., velocity, cumulative displacement, angular distortion, etc.). Some authors simplify the approach distinguishing between the type of buildings or foundations (Peduto et al., 2019, 2017b). Despite the high complexity of this evaluation, some general criteria and recommendations are given by some authors (Boscawen Burland and Wroth, 1975; Measor et al., 1956; Polshin and Tokar, 1957; Skempton and Macdonald, 1956). Finally, defining the acceptable damage a building can suffer according to its limit states is even more complex and depends on its destination of use and on economic considerations.

Here we use the spatial gradient of displacements as main damage inducing factor. The main objective of this methodology is to evaluate the intensity of the displacement spatial gradients and classify the buildings based on the potential damage level. Hence, we consider the relation between the intensity and the expected damage proposed by Polshin and Tokar (1957) and Skempton and Macdonald (2015). We follow the multiscale (multi-level pyramidal approach) perspective previously proposed by Cascini et al. (2013) and Peduto et al. (2017b, 2017a), as the methodology can be automatically applicable over wide areas (Figure *2*). Starting from a wide-area PSI displacement map as input (section 4.1), the first step is to derive a small-medium scale Active Displacement Areas map (Level 1) to localize the exposed areas and extract a

preliminary intensity information (section 4.2) based on the displacement statistics. The next steps are performed only at ADA-level and within a buffer surrounding the selected ADAs (ADA-buffer). This strongly reduces the computational time and allows to move to local scale level (Level 2). Then, the PS velocity values within the ADA-buffers are rasterized (section 4.3) and a slope map of the velocity values is finally calculated. The classified slope (section 4.4) constitutes the input for the two main outputs of the methodology: the Gradient Intensity Map (section 4.6), and the Potential Damage Map (section 4.7). Moreover, additional information is derived for a deeper analysis and interpretation: the gradient vectors, representing the direction of the gradients, and the gradient time series (section 4.5). Finally, a validation is performed through a test analysis of the damage prediction capability by comparing a Potential Damage Map and real damage inventory data, acquired through a field survey, and applying the damage classification approach proposed by Cooper (2008). The test performance is evaluated through the generation of ROC curves. All the steps after the ADA extraction were fully performed using ArcMap™ and can be reproduced in any Geographic Information System environment.

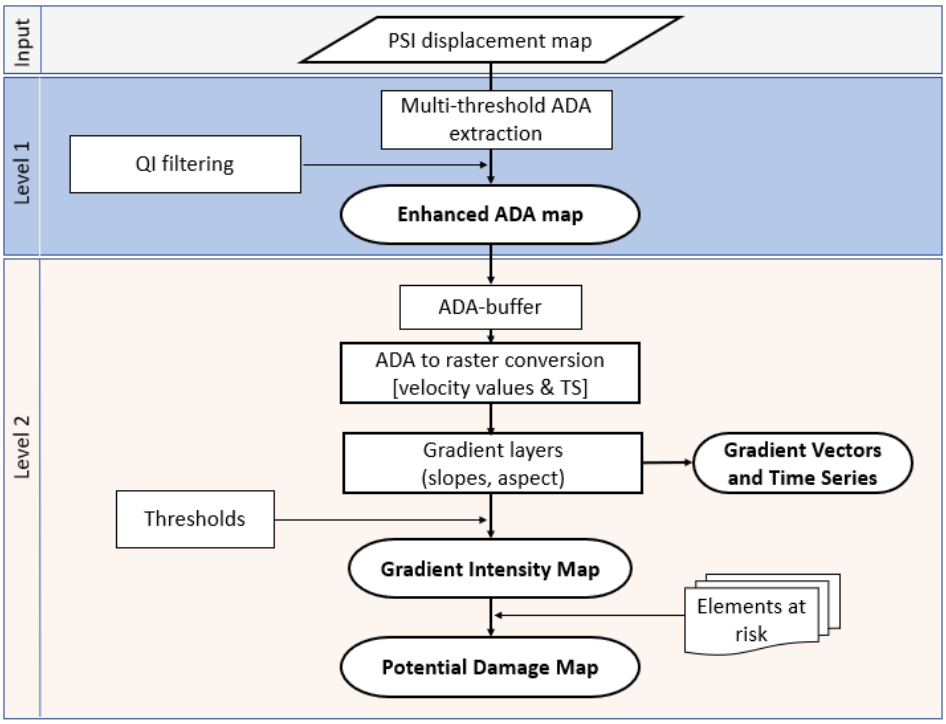

Figure 2 Methodology flowchart. In bold the main outputs.

4.1 PSI displacement map

The input of the methodology is a PSI displacement map, consisting in a set of Measurement Points (MPs) distributed over the processed area, where the mean annual velocity and the displacement time series (TS) are estimated. In this work, we have used the PSI processing software developed by the Geomatics Research Unit of CTTC (PSIG) to process a set of 230 Wide Swath Single Look Complex (SLC) images, acquired by the satellites Sentinel-1 A and B in ascending geometry. The processed data cover a period of 4.5 years (from 17/11/2015 to 06/05/2020), with a temporal sampling of one image every 6 days (with some exceptions of 12 days). The pixel footprint of Sentinel-1 data is approximately 4 by 14 m^2, and a full resolution processing was performed. We refer to Reyes-Carmona et al. (2020) for a short explication of main steps of the processing used here and to Devanthéry et al. (2019, 2014) for a more detailed description of the PSIG processing chain. It is worth underlining that the estimated velocities and displacements correspond to measures along the LOS direction. Hereafter, we always refer to LOS measurements when we talk about velocities and displacements. To remove the topographical component from the interferograms, the 3-arcsec Shuttle Radar Topography Mission (SRTM) Digital Elevation Model (Farr et al., 2007), freely provided by NASA, was used.

4.2 Level 1: ADA Detection and selection

The detection and extraction of the ADAs was performed with the methodology explained in Barra et al. (2017) using the ADAFinder software (Navarro et al., 2020, 2019; Tomás et al., 2019). Each ADA polygon synthesises the most significant information of the movement: the mean, minimum and maximum velocity, the number of PS that forms the moving area and the accumulated displacement. It also provides a Quality Index (QI) that represents the noise level of the TS within each ADA. The QI is crucial for non-expert users to understand the level of reliability of each moving area and to eventually exclude the noisier ones from the analysis. The algorithm of ADAFinder is based on a simple concept that was already proposed by Bianchini et al. (2012), Meisina et al. (2008) and Notti et al. (2014): if the number of active contiguous PSs exceeds a predefined threshold, those PSs are considered a cluster and extracted as an ADA. What does

active and *contiguous* mean? These are two conditions defined by the user. For that purpose, the user must specify two key factors: the proximity distance (in terms of radius around each PS) to consider two points as contiguous, and the Velocity Threshold (VT) to classify a point as active. The first factor is usually based on the resolution of the used SAR data. For Sentinel-1 data, Barra et al. (2017) proposed to set this radius to 26 meters: this value was used in several applications and has empirically confirmed to be effective. The Velocity Threshold (VT) is based on the standard deviation of all the velocity values of the displacement map (V_stdev), considering the V_stdev over wide areas as an indicator of the global level of noise (Barra et al., 2017). The user can decide a factor (F_stdev) that is multiplied by the V_stdev to derive the VT to be used. The lower the VT, the higher the noise included in the areas, whereas if the VT is high the extraction is more restrictive and slower areas are not detected. The presence of noise within each ADA is reflected by the QI value. To avoid these limitations and improve both the detection capability and the QI characterization of the moving areas, we propose a multi-VT ADA extraction. Thus, ADAFinder is used iteratively three times, changing the F_stdev, and if an area is extracted with more than one threshold the best calculated QI will be assigned to that area, being the most representative. The selection of the F_stdev depends on the analysis being performed and on the characteristics of the study area. In this work, we used the F_stdev values of 1, 1.5 and 2. Consequently, we could detect moving areas characterized by slower movements, without losing any information. Finally, based on the QI, which entails 4 classes (from class 1, the most reliable, to class 4, the most unreliable), all the unreliable ADAs (QI=4) were removed and not considered in the next steps.

4.3 ADA to raster conversion

A buffer of 150 meters is created around each ADA, then used as a mask polygon for the next steps, yielding lower computational charge and clearer results. The buffer allows including in the analysis the PSs that are in the surrounding areas of the ADA, which can be stable, with a lower velocity or isolated with respect to the main moving cluster. Moreover, it is common that the stronger gradients of movements are expected to be located at the borders of the main movement, especially at the interface between different lithologies or

where a structural or geomorphological element is present (e.g. a landslide crown). The PSs within the ADA-buffers are rasterized to have a regular grid information. This is done for the displacement accumulated at each acquisition time (derived from the TS) and for the velocity values. Since the PS information is spatially sparse, we can have pixels with more than one PS, and pixels with no PS. For the first case, the average of all the PSs that fall inside the pixel is assigned, whereas for the second case, a smooth and linear interpolation is done assigning the mean value between the surrounding pixels. The interpolation is done applying the *focal statistics* algorithm only for the empty cells surrounded by values, by using the *raster calculator* tool. Let us call R-DEFO(i) all the rasterized displacements (mm) at the i^{th} image, and R-VELO the rasterized velocity (mm/year). It is worth underlining that the interpolation is not continuous for the whole area, as the interpolation of distances longer than 100 m is avoided. The raster cell-size was set at 22 m, based on the estimation of the general point density within the ADAs.

4.4 Gradient layers

The *slope* tool calculates for each pixel the maximum rate of change (gradient) of displacement between the eight neighbouring pixels (Burrough and Mcdonnell, 1998). The *slope* of the mean velocity (R-VELO) is calculated to assess the mean velocity gradient (from now, SL-VELO), which is the main information used to derive the intensity and the potential damage maps. The slope of each displacement raster image (R-DEFO(i)) is calculated to assess the gradient of the displacement time series (from now, SL-DEFO(i)). The slope is calculated as percent rise: the output values are the percentage of differential displacement (Δ_Disp.) per distance (L) unit (percent of slope = Δ_Disp./L*100). Moreover, the *aspect* of the velocity is calculated to visualize the main direction of the maximum spatial gradients (hereinafter referred to as AS-VELO) and will be used to visualize the gradients as vectors.

4.5 Gradient Vectors and Time Series

A point shapefile is generated using *raster to point* tool: the points are located at the centroid of the pixels of the gradient layers, which are perfectly aligned (i.e., *snapped*). The information of all the layers of the correspondent pixel is transferred to the point shapefile attribute table through the *sample* tool. The sampled

layers are: R-VELO, SL-VELO, AS-VELO, and all the slopes SL-DEFO(i) ordered in time. Sampling the SL-DEFO layers allows reconstructing the temporal evolution of the gradients (Δ-TS) at each point. The AS-VELO allows us to represent the point shapefile as vectors, where the direction of the arrow is determined by the AS-VELO angle being the direction of the main spatial gradient at that location.

4.6 Gradient Intensity Map

The Gradient Intensity Map corresponds to the classified SL-VELO layer. The SL-VELO itself can be considered as an intensity map in terms of angular distortions ($\beta = \Delta\_Velocity/L$, where β is the angular distortion). Nevertheless, to have an operational map useful at medium to local scale, we need to pass from a series of continuous numbers to a qualitative classification of intensities that can be translated to potential damage classes. To do so, we need to set specific thresholds. Many authors tried to assess general thresholds for settlements of building (Boscawen Burland and Wroth, 1975; Measor et al., 1956; Polshin and Tokar, 1957; Skempton and Macdonald, 1956). Others (del Soldato et al., 2019; Peduto et al., 2017a) start from a damage inventory, based on field surveys, to find the relation between the intensity parameter (e.g. velocity, differential settlements, etc.) and the observed damages (fragility curves). Here we used a data-driven classification; specifically, the thresholds were based on the cumulative frequency distribution of the SL-VELO. Five classes were used, setting the four thresholds at the values corresponding to the cumulative frequencies of 50% (second quantile), 75% (third quartile), 85% and 95%. Then, we refer to Skempton and MacDonald (1956) to attribute to each threshold a meaning in terms of potential damage intensity. These authors recommend avoiding angular distortion higher then 1/1,000 (β_1) or 1/500 (β_2) and establish some general limits of the angular distortion that potentially produce cracking in walls and partitions ($\beta_3 = 1/300$), or that cause structural damage ($\beta_4 = 1/150$). Assuming a constant gradient rate, the thresholds of annual gradients fixed in this work correspond to the accumulated angular distortion β_1, β_2, β_3 and β_4 over a period of 25 years (see Section 6.2). The two last and most critical thresholds are smaller than β_3 and β_4 by a caution factor.

4.7 Potential Damage Map

A shapefile of the buildings was used to generate the exposed elements Potential Damage Map. The buildings are classified based on their position with respect to the Gradient Intensity Map. When a building overlaps more than one pixel with different values of displacement intensity gradients, the maximum one is used. The vector layer of the buildings was acquired from the OpenStreenMap database.

5 Validation and threshold assessment

A field survey was performed to classify the buildings based on visible external damages. The classification proposed by Cooper (2008) was used. This author categorizes structural damage due to subsidence and landslide phenomena and presents a scheme including a description and classification of fractures and scarps detectable on the ground surface. Seven categories are proposed ranging from 1, which is barely perceptible, through 5, which is very severe with considerable damage, to 7, which is total collapse. The surveys have been carried out in the resorts of Los Almendros (both in May 2019 and July 2020), Alfa Mar (in May 2019), Cerro Gordo (July 2020) and Punta de la Mona (November 2021). For Marina del Este we refer to the damage inventory map generated in January 2015 (Notti et al., 2015). Moreover, evidence of other damages was mapped as both linear and punctual annotations, such as road cracks and potholes or cracks on walls.

5.1 Damage prediction test - ROC curves

To validate the damage prediction accuracy of the proposed method, we performed a damage prediction test, comparing the intensity values of the Potential Damage Map with the damage inventory of the three resorts of Los Almendros, Cerro Gordo, and Alfa Mar. Because of their unfavourable orientations, Marina del Este and Punta de la Mona have been selected to be analysed through a slightly different approach (see the discussion section). For this reason, they have been excluded from the prediction test analysis. The test was done and evaluated through the generation of a series of ROC curves. A ROC curve is based on confusion matrixes generated by using several thresholds that set the difference between a positive (presence

of damage) or negative (absence of damage) prediction. A ROC curve describes the behaviour of the true-positive rate as a function of the false-positive rate, which is generated by using different thresholds that set the difference between a positive (presence of damage) or negative (absence of damage) prediction. For each chosen threshold value, one will have a different performance in terms of ability to lead to a positive prediction where the building is effectively damaged (true-positive result), and a negative prediction in case of not damaged building (true-negative result). This can be evaluated with a simple contingency table, where the numbers of true-positive (TP), false-positive (FP, i.e., positive prediction in case of no-damaged building), true-negative (TN) and false-negative (FN, i.e., negative prediction in case of damaged building) are visualized. To compare different models and have a more comprehensive assessment, we can use the ROC curves, where the true-positive rate (TPR=TP/(TP+FN)) are plotted against the false positive rate (FPR=FP/(TN+FP)) for each possible threshold. The discriminating capacity is then proportional to the extension of the area under the ROC curve (Area Under Curve, AUC). The greater the AUC, the greater the probability of having a true-positive result over the probability of having a false-positive result. A value of AUC of 0.5 occurs if the ROC curve falls on the diagonal of the diagram, indicating that the model has no discriminatory capability: independently from the used threshold, the percentage of true-positives equals to the percentage of false-positives. As a rule, an AUC of 0.5 indicates no discriminating capability, whereas an AUC between 0.6 and 0.7 relates to a poorly discriminant model, an AUC between 0.7 and 0.8 is considered acceptable, an AUC between 0.8 and 0.9 is considered excellent, and an AUC higher than 0.9 is considered outstanding. Through the AUC, we evaluated the prediction performances of the Potential Damage Map, and how it changes depending on the damage level. Moreover, the percentages of TPR and FPR were used to assess the optimal threshold of the test, as the one that maximizes the difference TPR-FPR, having the highest discriminatory capability.

6 Results

6.1 Level 1: PSI displacement and ADA maps

The PSI processing allowed to obtain a displacement map (Figure 3-A) consisting of around 215,000 MPs, with information on the mean annual velocity and on the displacement time series for each point, over a total area of about 700 km^2. The standard deviation of the velocities resulted in 2.9 mm per year. This value was used to assess the general noise level of the displacement map, always considering that noise level changes within the AOI depend on the local surface conditions and characteristics of the land cover. From this map, the multi-threshold ADA extraction and QI assignation was performed: the final number of ADA for each QI class is resumed in Table 1. Figure 3-B shows the ADAs obtained after excluding the ones with a QI class equal to 4 (not reliable areas). This resulted in a total of 175 ADAs that were selected for the next steps of the methodology.

Table 1 Number of ADAs extracted for the Quality Index classes 1, 2 and 3.

	Description	**Number of ADA**
QI=1	Reliable	55
QI=2	Reliable with some noise	72
QI=3	To be checked	48
TOT		**175**

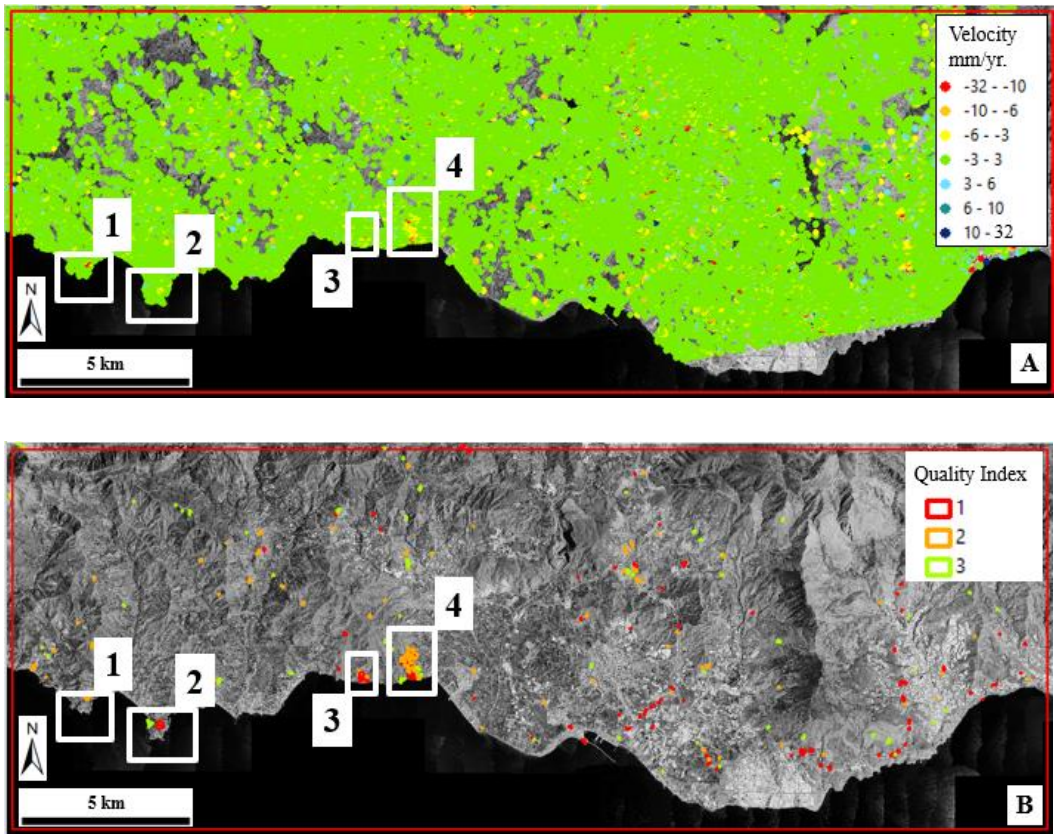

Figure 3 A) PSI displacement map obtained over the AOI, showing the annual mean velocity. B) ADA map obtained from the PSI displacement map, showing the areas extracted through the multi-threshold approach together with their quality index. The rectangles 1, 2, 3 and 4 show the location of the four areas selected to present the results of the Second Level of the methodology.

6.2 Level 2: From ADA to Gradient Intensity Map

To show the results at a detailed scale, we focus on the four areas of interest (Figure 1, Figure 3): Cerro Gordo (1); Punta de la Mona Promontory (including Punta de la Mona and Marina del Este) (2); and Monte

454 de los Almendros (3).

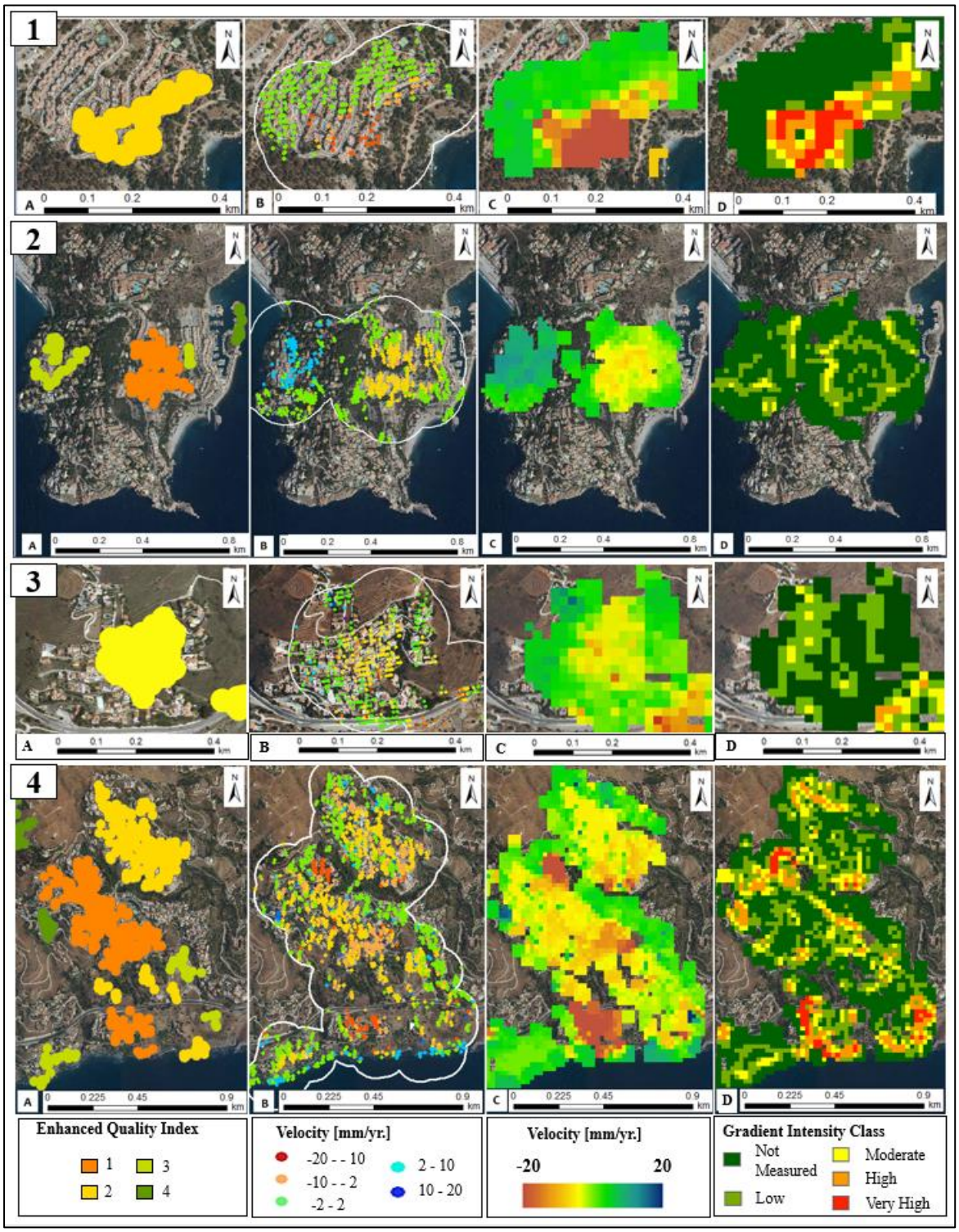

455

456 *Figure 4*-A shows the extracted ADAs classified according to their QI.

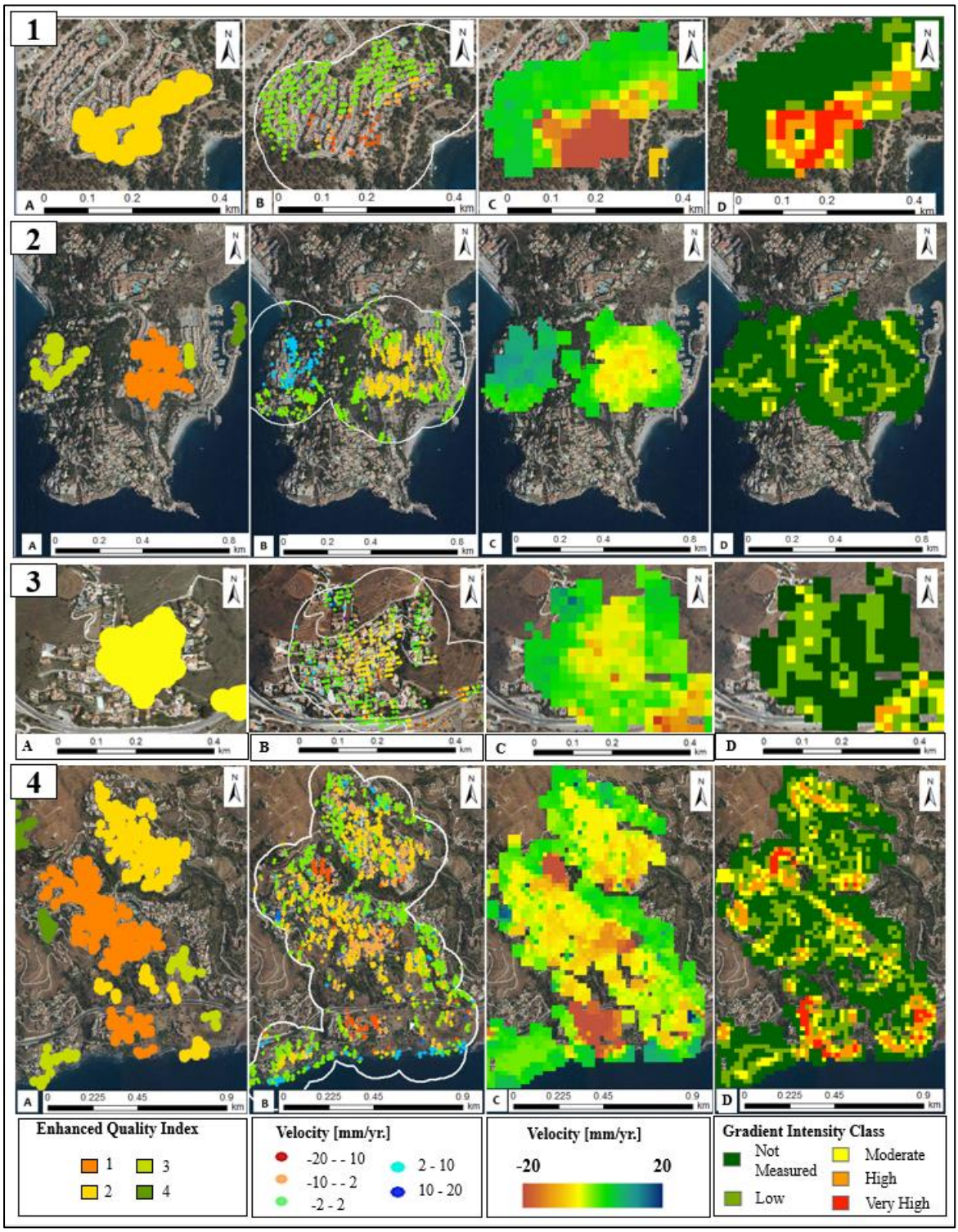

457

458 *Figure 4*-B shows the ADA-buffer areas generated with a distance of 150 meters from the selected ADAs,

459 and the PSs of the displacement map that fall inside those areas. Figure 4-C shows the rasterized velocity

460 map. Figure 4-D shows the Gradient Intensity Maps. Table 2 shows the upper thresholds (third column) of
461 each class in terms of velocity gradients in % (mm*yr.-1*m-1), the relative cumulative frequencies, the
462 angular distortion (β) reached in 25 years, assuming the gradient rate does not change in time, the reference
463 value from Skempton and MacDonald (1956), and the cautious factors.

464 *Table 2 Proposed classes for the Gradient Intensity Map and their meaning in terms of Angular Distortion expected in 25 years.*
465 *The reference values of angular distortion are referred to Skempton and MacDonald (1956).*

Class number	**Intensity Class**	**Annual Gradient % ($mm*yr.^{-1}*m^{-1}$)**	**Cumulated Frequency %**	**Angular distortion (β) in 25 years**	**β reference values***	**Factor**
0	Not measured	≤ 4	50	≤ 1/1,000	≤ 1/1,000	1
1	Low	8	75	1/500	1/500	1
2	Medium	12	85	1/333	1/300	1/1.1
3	High	20	95	1/200	1/150	1/1.3
4	Very high	> 20			>1/150	

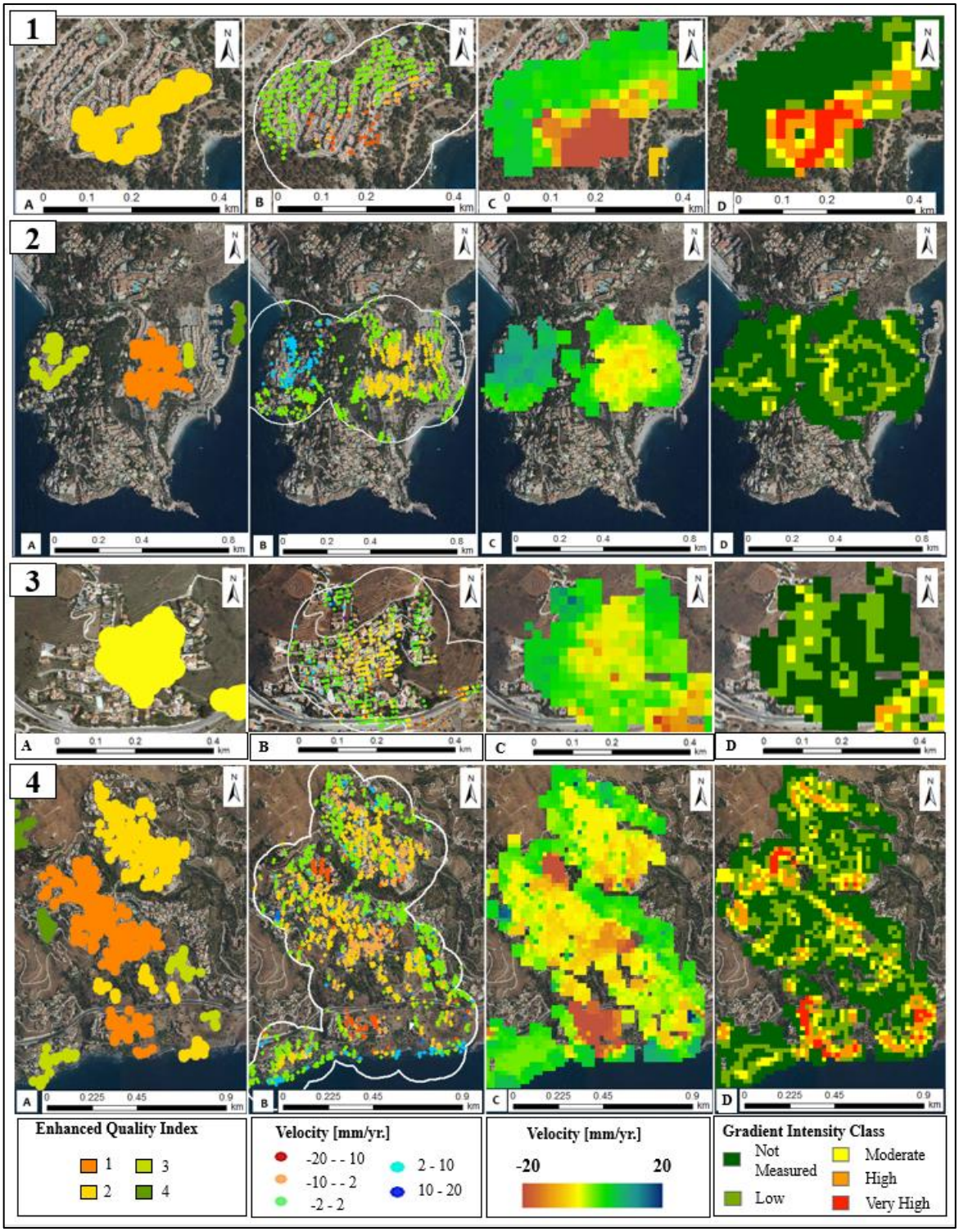

Figure 4 Results over the four local areas selected for the analysis: Cerro Gordo (1), Punta de la Mona Promontory (2), Alfa Mar (3) and Monte de los Almendros (4). For each area, the results of the main steps of the Methodology are showed: ADAs extraction (A), ADA-Buffer masking (B), rasterization and interpolation (C), and the Gradient Intensity Maps (D).

6.3 Gradients vectors and Time Series

Starting from the gradient maps, we can derive additional information useful for representation and analysis purposes. Here we present the case of Cerro Gordo. Each point of Figure 5 represents the centroid of a pixel. For each pixel we can visualize the following information (Figure 5-A)Figure 5: the colour of the point represents the velocities as calculated in the rasterization step (R-VELO); the arrow represents the main direction of the velocity gradients (AS-VELO) and its colour the intensity class in terms of annual rates of gradients (SL-VELO). Additionally, for each point we can visualize both the time series of displacements (TS, derived from R-DEFO(i)), and the time series of differential displacements (Δ-TS, derived from SL-DEFO(i)). Figure 5-B shows a detail of the area within the wite frame of Figure 5-A, the numbers refer to the TS of Figure 5-C. In Figure 5-C, we see an example of Δ-TS of the central point (2), and we compare it with the displacement TS of the same point with respect to its neighbour points 1 and 3, located on the direction of the main gradient of point 2. The displacement was spatially uniform (points 1, 2 and 3 were moving together) until March 2018, when the three points accelerated and started moving with different rates, generating differential displacements. Thus, the Δ-TS allows here to determine the time when the stress conditions of the building changed. Figure 5-D shows a profile of the velocity (Figure 5-E) along the main direction of the movement (the arrows represent the gradients). The map of gradients and vectors allows a fast interpretation on the movement characteristics (Figure 5-F): the distribution of velocities and gradients along the a-b profile is consistent with the presence of two main crowns of landslides, with a rotational component that would justify both the two points of faster movement along the slope, and the gradient directions going in the opposite direction of motion.

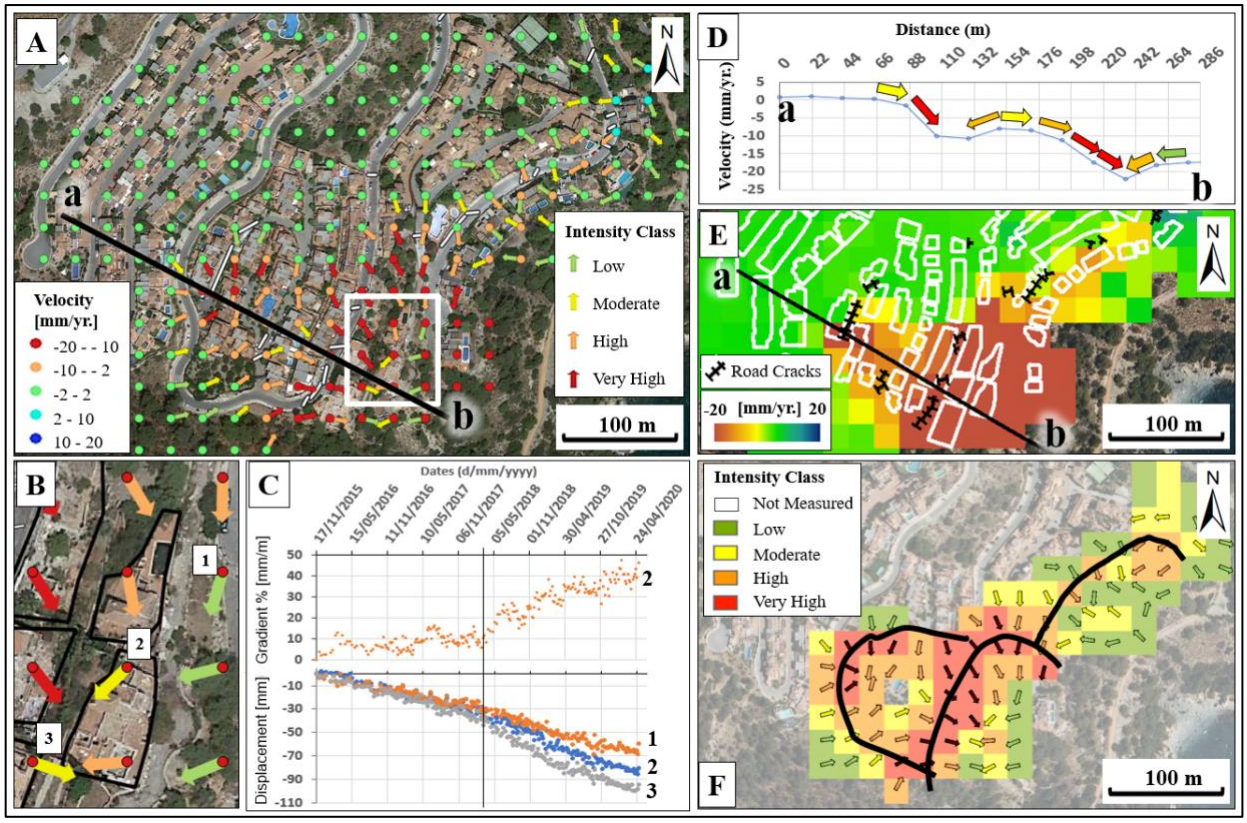

*Figure 5 Results over the area of Cerro Gordo. Figure A shows the Map of Gradient Vectors (arrows) classified according to their intensity class; the points represent the displacement velocities (mm*yr.$^{-1}$). The area enclosed by the white rectangle is shown in detail in Figure B, where the black polygons represent the buildings. The TS of displacements (mm) of points 1, 2 and 3, together with the Δ-TS (mm*m^{-1} %) of point 2, are shown in image C. Figure D shows the velocity profile and the arrows above represent the consequence gradients of velocity, along the line a-b showed in figures A and E. Figure E shows the rasterized velocity, together with the polygon of the buildings (in white). Figure F shows the gradient intensity map, together with the gradient vectors. The black lines represent an expeditious interpretation of the movement crowns, only based on the gradient intensity map and vectors.*

6.4 Potential Damage Map

The Gradient Intensity Map is used to generate the map of Potential Damage for the exposed elements. In Figure 6 we use again the case of Cerro Gordo to visualize: the PSI displacement map (A) superimposed over the building's polygons (in black); the derived raster of gradient intensities (B); the damage inventory (C); and the Potential Damage Map (D). The red rectangle shows an example of buildings located in a critical border position, where the result depends on the rasterization resolution and pixel positioning. The

yellow circle shows an example of time-related incongruity between the potential damage and what is visible on the field at the time of the survey. If we compare our damage inventory map (ref. date July 2020) with the one produced by Mateos et al., 2017 (ref. date January 2016), we see that the same building was classified with a moderate damage severity in 2016, whereas it did not show any damage in 2020. Thus, the damage state has changed probably after stabilization or reconstruction interventions realized between 2016 and 2020: it is now counted as false positive case. It is worth to notice that damages on roads or low walls, which have a direct response to the differential movements and overlap quite well the areas classified with a moderate, high, or very high gradient intensity, are frequently located in the vicinity of false positive predictions. The blue square shows a false negative case, located in this case at the border of the PSI displacement map (Figure 5 A): no measurement points were retrieved at the eastern and southern sides of the buildings; thus, we can calculate the gradient by using partial information only, which results in a less reliable prediction.

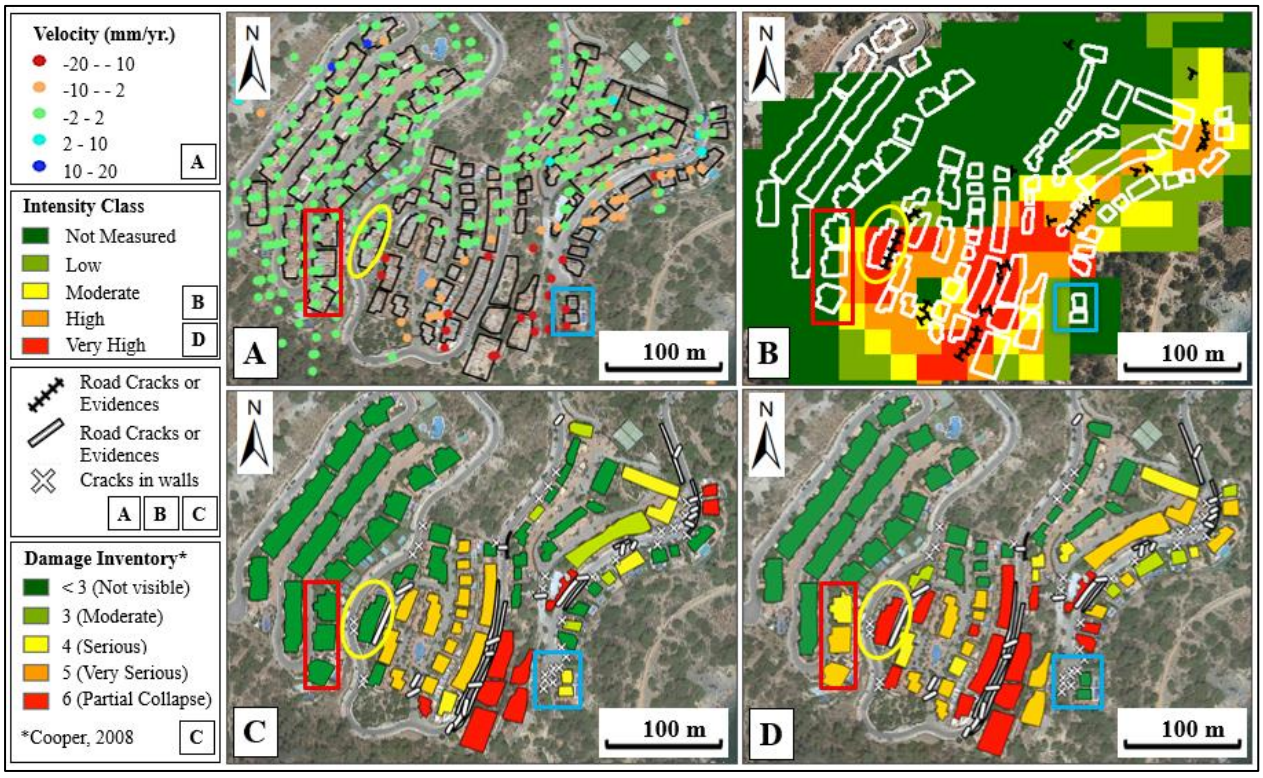

Figure 6 Results in Cerro Gordo. A) PSI displacement velocity map (input of the methodology); B) Gradient Intensity Map (output of the methodology), superimposed with the polygons of the buildings (white) and the road cracks mapped on the field (black lines); C) Damage inventory map done through field survey; D) Potential Damage Map (output of the methodology).

6.5 Validation and threshold assessment

6.5.1 Damage Inventory Map (field survey)

As described in the previous sections, the damage Inventory Maps were based on Cooper (2008). Table 3 summarizes the number of the buildings classified in each class, for each urban area. Figure 7 shows some pictures taken in Cerro Gordo to explain some examples affected by different types of damage. The inventoried buildings of Alfa Mar, Cerro Gordo and Monte de Los Almendros were used as test dataset to validate the prediction capabilities of the Potential Damage Map.

Table 3 Number of building inventoried over each urban area for each class of damage (Cooper, 2008), and the total numbers used for the ROC analysis.

Urb. / Class	Alfa Mar	Cerro Gordo	Almendros	Totals for ROC Analysis	Punta Mona	Marina Este	TOT
<3 (Not visible)	68	40	401	**509 (~ 80%)**	136	104	749
3 (Moderate)	17	5	49	**71 (~ 11%)**	21	39	131
4 (Serious)	5	6	9	**20 (~ 3%)**	7	5	32
5 (Very serious)	1	15	3	**19 (~ 3%)**	0	0	19
6 (Partial collapse)	2	9	3	**14 (~ 2%)**	1	0	15
TOT	93	75	465	**633**	165	148	946

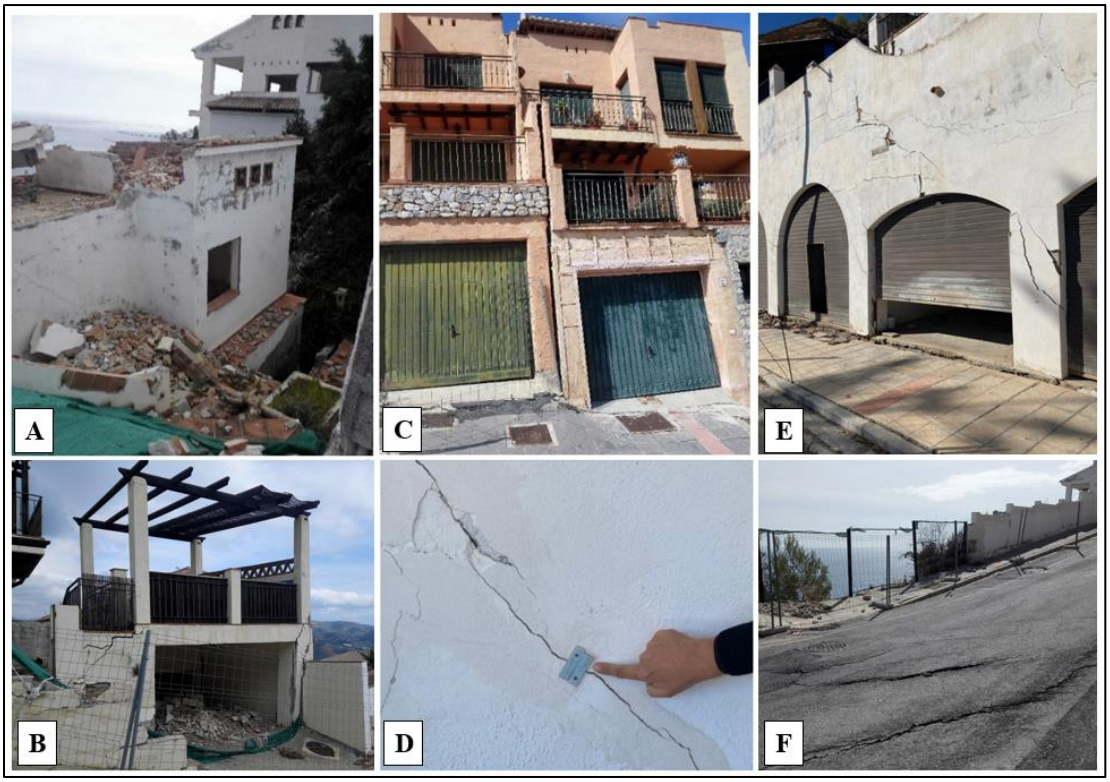

Figure 7 Examples of landslide-field evidences and damages in Cerro Gordo. Images A and B belong to class 6 (partial collapes), Image C is is an example of class 5, a very serius damage, with a distinct crack (separating two bloks) and tilts affecting the garages. Images D and E are examples of wall cracks belonging to class 4 (serius damage); Image F shows cracks and deformations on the street.

6.5.2 Damage Prediction Test (ROC analysis)

In this section, we try to answer the following questions: is differential displacement a discriminant parameter for potential damage detection? In such a case, for which classes of damage? And which are the most suitable thresholds to used?

Figure 8-A shows a graph with four ROC curves generated by considering as "damaged" four selections of the classes: starting from only the most severe (class 6), and then including for each curve the next class, i.e., the class corresponding to the next lower damage level. This is done to analyse how the prediction capability changes depending on the damage severity levels. The numbers next to the curves are the thresholds used to generate the ROCs (see section 6.1) and represent the gradients of velocity (mm $yr.^{-1}m^{-1}$,

in %) used to classify the buildings as damaged or not-damaged. The ROC curves seem to approach the diagonal, as we introduce classes of lower damage level. We can see that the prediction capabilities are acceptable and almost the same if we consider only the class 6 (AUC_6=0.74) or classes 5 and 6 together ($AUC_{5,6}$=0.73). The AUC slightly decrease ($AUC_{4,5,6}$=0.68) if we also introduce class 4, but in this case the test is poorly discriminant even though the AUC is about 0.7. The "belly" of the curve indicates that the discriminatory capability starts to improve using thresholds higher than 4, as the curve starts moving away from the diagonal. Finally, the performance is strongly affected by the inclusion of class 3, with a ROC curve that is very close to the diagonal regardless the used threshold ($AUC_{3,4,5,6}$=0.65). Figure 8-B shows a similar analysis performed by using as intensity value the absolute values of the velocities instead of gradients. We see that the prediction capability of the velocity abruptly decreases from acceptable (AUC_6=0.77) to poorly discriminant ($AUC_{5,6}$=0.59) as we move from considering only class 6 to considering the classes 5 and 6. This means a good discrimination only for the class 6 (partially collapsed), which is not satisfactory for preventing purposes. Therefore, it is evident that the use of gradients as intensity values to predict damage, provides a higher discriminant capacity than the use of velocities.

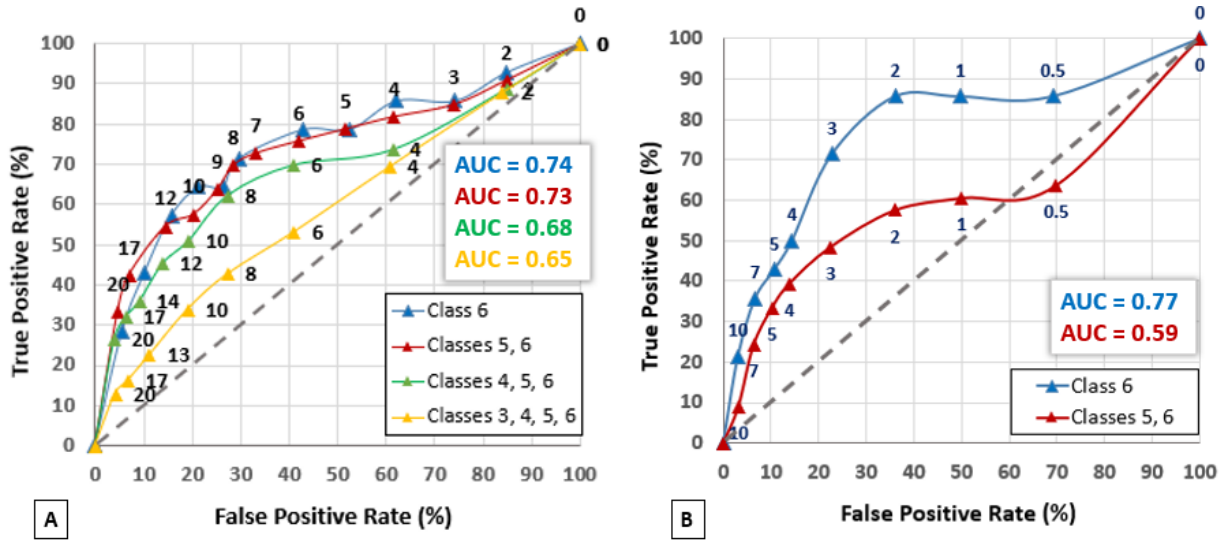

*Figure 8 ROC curves generated with the same test sample, considering the gradients (A) and the velocities (B). The different curves are generated considering as damaged only a sub-selection of classes. The numbers are the thresholds used to plot the curves, in % [mm*yr.$^{-1}$*m^{-1}].*

6.5.3 Threshold assessment

In the following, we will refer to the threshold values of velocity gradients just as percentages (%). Figure 9 shows the information derived from the confusion matrices used to generate the ROC curves. The figure shows how the percentages of TPR, FPR and FNR vary depending on the threshold, as well as the inter-relation between them. Each graph refers to one class, meaning that we consider as damaged only those buildings inventoried within that specific class. Note that we are talking about binary prediction, where no-damage is a negative prediction and damage is a positive prediction. Given the relation between TPR and FNR (FNR= 1-TPR), the TPR and FNR lines are symmetric with respect to 50%. For each point of the curves, the prediction is positive for all the buildings with gradients higher than the threshold and negative for the ones with gradients lower or equal. The double arrows show the threshold that generates the maximum Discrimination Level (DL=TPR-FPR) we have until the FNR are lower than the FPR. The Maximum DL (Max_DL) is almost the same for damage classes 6 and 5 (Max_DL≈40%), while for class 4 it decreases by half (Max_DL≈20%), whereas it is null (TPR≈FPR) for the class 3 at any threshold. As shown in the figure, for classes 6 and 5, Max_DL is reached with a threshold of 8% (gradients higher than 8%). This value represents the optimal threshold for the two highest damage levels. For class 4, the optimal threshold would be 6%. Nevertheless, if we look at threshold 4, we see that the TPR and FPR do not change and is associated to an increase of DL. Furthermore, threshold 4% represents a TPR of around 80% for Class 5 and of around 85% for Class 6. Since FPRs are probably overestimated (and, consequently, the DL underestimated), we prefer to maintain the first threshold (a value of 4%), as it leads to higher TPR and FPR, and lower FNR, and provides a first aware class (of low intensity).

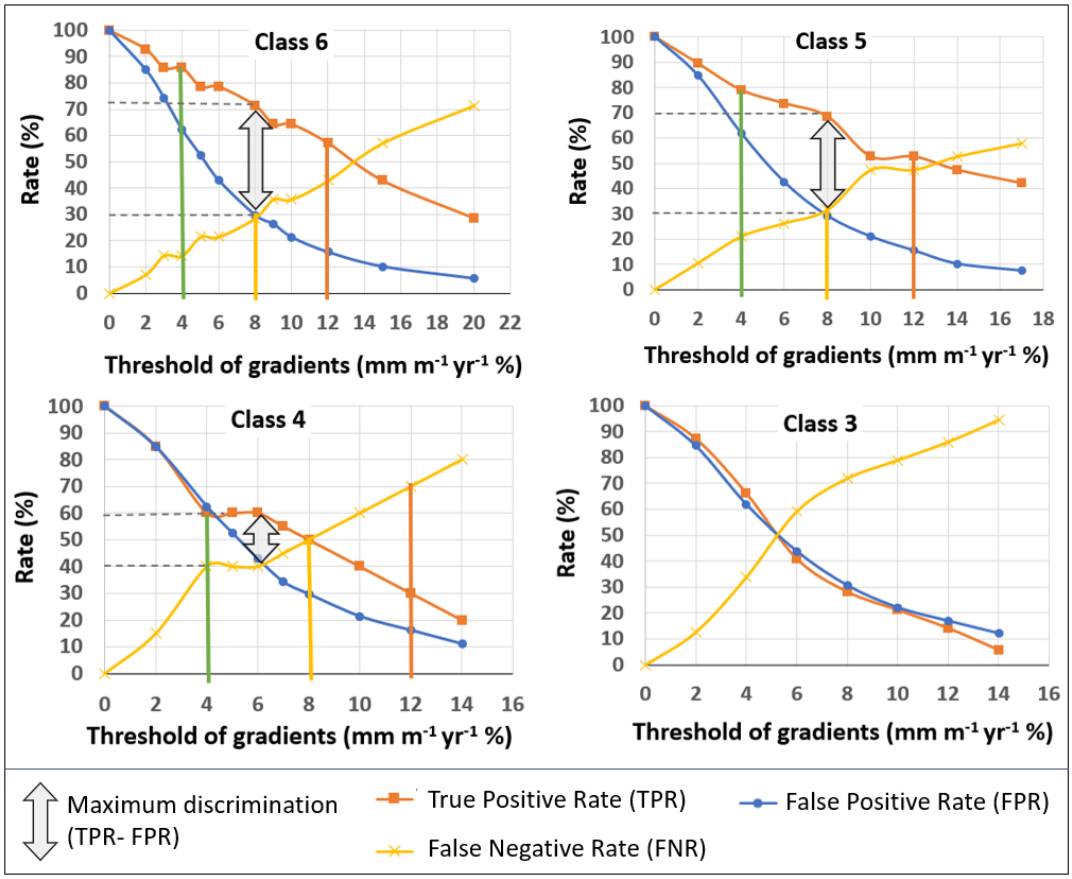

582

583 *Figure 9 Graphs showing the behaviour of the test predictions depending on the threshold, for each damage class. The orange, blue*
584 *and yellow curves represent respectively the True Positive Rate (TPR), the False Positive Rate (FPR) and the False Negative Rate*
585 *(FNR). The arrows show the thresholds corresponding to the maximum discrimination levels*

586 # 7 Discussion

587 The focus of the proposed methodology is to extract, from a regional-scale PSI displacement map, a series
588 of maps useful for medium to local scale applications. The extracted information is related to the intensity
589 parameter of differential displacements, which allows us to locally detect the areas where an exposed
590 element is more likely to be already damaged or prone to be damaged in the future, provided that the external
591 action persists. The main advantages of the procedure are that it can be applied semi-automatically over
592 wide areas, independently from the type of movements, and that it is totally based on freely available remote
593 sensing data. The methodology has been applied here over an area of around 700 km^2 located in the province

of Granada (South of Spain): from the extraction of the most significant ADAs to the generation of the Gradient Intensity and Potential Damage Maps. The ADA map represents the first-level information, which allows localizing exposed areas and, based on the velocity statistics, assigning them a first-level of intensity. The ADAs allow reducing in an automatic way the volume of information to be processed by the user. In this case, this approach has allowed to pass from more than 200,000 MPs to just 175 ADAs, most of them belonging to a common moving area. This strongly reduces the interpretation time and increases the operational use of PSI for small-scale territorial management purposes. Through the ADA-buffer we can automatically work only over the extracted ADAs, without losing boundary information, and strongly reducing the computational time and data storage. The main second-level product of the methodology is the

603 gradient intensity map (

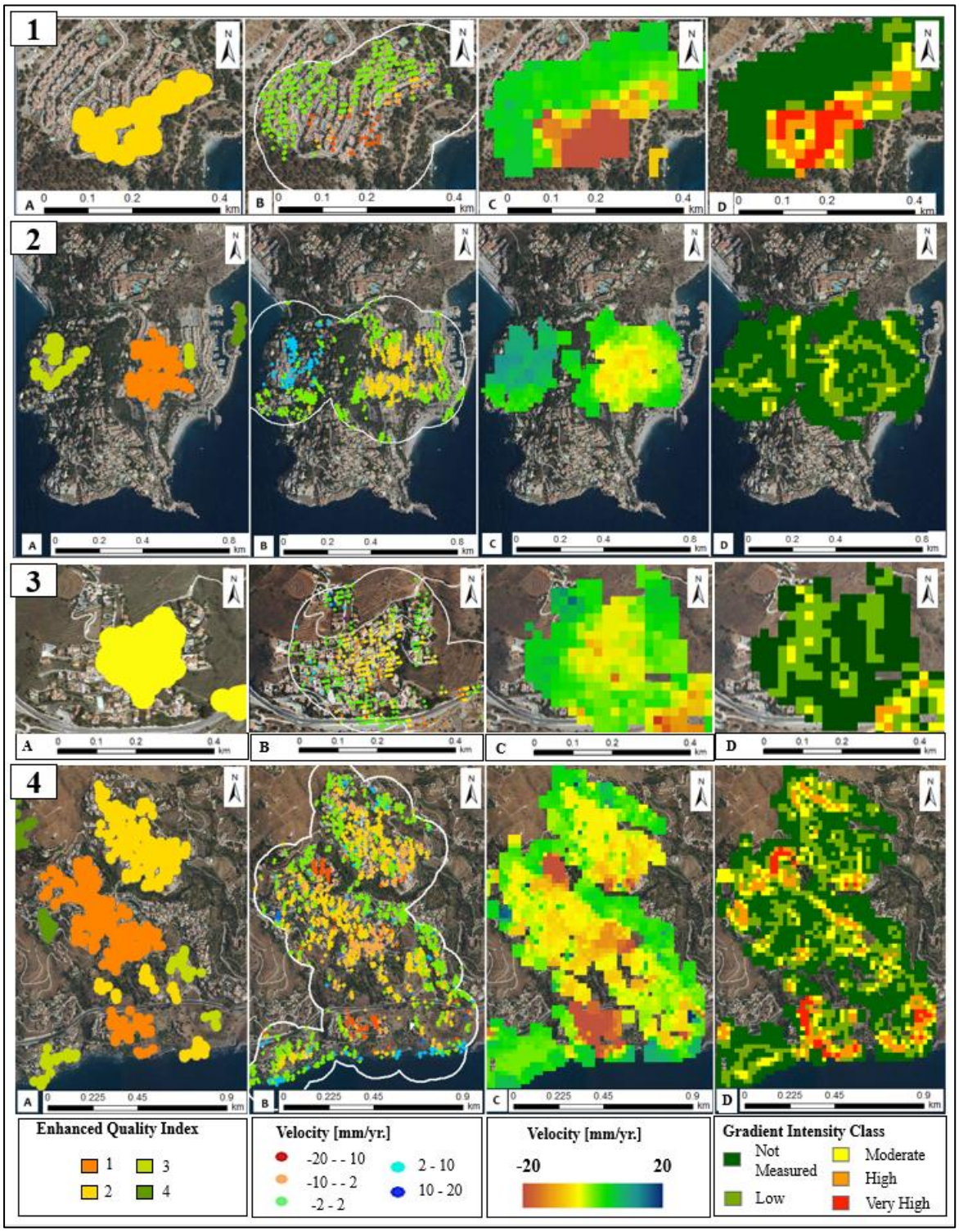

604

605 *Figure 4*-D). Once an exposed area is localized (through the ADA map) it is possible to perform a local

606 analysis to visualize how the intensity, in terms of spatial gradients of movement, is distributed in space.

607 Some authors use the velocity (or the total displacement) as intensity value, instead of using the differential
608 velocity (or the differential displacement), as proposed in our work. Through the damage prediction test
609 performed and the comparison of the ROC curves carried out (section 5.1), it has been proven that
610 differential movements are much more discriminant than velocities for detecting damage prone areas.
611 Moreover, the gradients can highlight some characteristics of the movement, for example indicating the
612 boundaries of primary and secondary landslide bodies (Figure 5). The gradient vectors and time series
613 provide essential information for further analysis. The gradient TS, if regularly updated by applying
614 continuous monitoring and implemented in an automatic TS trend change detection (Raspini et al., 2018),
615 could allow a prompt detection of changes in the stress conditions of the buildings (Figure 5). The
616 directional vector has not only a representation purpose, but it also gives valuable information to determine
617 the relationship between the main stress direction and the building geometry. The expected differential
618 displacement suffered by a structure (and thus the damage level) is different if the direction of the angular
619 distortion is parallel to the shorter or longer side of the building. This aspect has not been considered in this
620 work and could be an added element for an improved Potential Damage Map. The proposed Potential
621 Damage Map together with the Gradient Intensity Map, are two useful maps to support field surveys and
622 perform deeper analyses.

623 Note that assigning an intensity class to each building based on its position with respect to the gradient map
624 (Figure 5-b), would be a first step towards the vulnerability assessment. However, to make a more complete
625 vulnerability classification, we should add additional information such as year of construction, eventual
626 securing interventions, geometry measurements, construction type and material, foundation type, and
627 destination use. The use of the annual velocity gradients (instead of total accumulated gradients) allows to
628 estimate the values over different times. Based on their classification and considering the values provided
629 in previous studies (Skempton and Macdonald, 1956), we could associate a level of expected damage (e.g.,
630 cracks or structural) to each class.

631 The results of damage prediction test, shown in Figure 8 and 9, allowed us to derive some considerations
632 about the prediction capability of the methodology for each level of damage. The Potential Damage Map
633 proved to be unable to predict the test samples belonging to Class 3 (moderate damage): independently from
634 the threshold, the spatial gradients behave as a random classifier, with no ability to discriminate between
635 moderate-damage and no-damage. For Class 4, the test revealed a poor discrimination capacity, whereas for
636 classes 5 and 6 (i.e., the higher damage classes), the discrimination capacity was found to be acceptable.
637 Surely, the different classes have a different statistical significance depending on the sample size, which is
638 drastically reduced from class 3 to class 6. Nevertheless, note that even though the size of the classes 4 and
639 5 is almost the same (20 and 19, respectively), the results obtained for both classes in terms of TPR/FPR are
640 strongly different. Therefore, it is reasonable to think about other aspects conditioning the prediction
641 capabilities of the methodology. In this sense, the uncertainties associated to the damage field-observations
642 within each class, represent another important factor, which could have an impact on the results of the
643 prediction capabilities analysis. Since the damage inventory was prepared by visual inspection from outside
644 the buildings, the lower the damage level the more the observation is subjected to variables like visibility
645 and recognisability. Moreover, the building external status can be altered, fixed, or occulted (e.g., fissures
646 or small cracks can be easily filled and painted). Furthermore, the damage classification is also the result of
647 a subjective evaluation carried out by the operator. Finally, it must be taken into account that lower damage
648 levels are expected to be related to lower displacement intensity gradients, which are more difficult to be
649 detected by the PSI technique, especially when they are at or below the precision limit of the technique. By
650 contrast, a stronger damage level is more evident and more difficult to be repaired or hidden. Given the
651 multiple elements that can create a false positive, the evaluation of the methodology should focus on the
652 false-negative rates. Whereas false positives could be interpreted as potential damage areas, negative
653 predictions should be read as unmeasured rather than no-damage. We have seen that false negatives are
654 related to the intrinsic limitations of both the PSI technique (namely geometric limitations, absence of
655 measurement points or non-precise geo-localization), and the methodology. The latter are mainly related to
656 the rasterization and interpolation process (Figure 6). Based on the analysis of the thresholds (Section 6.7),

we have seen that using the optimal gradient threshold of 8 % (mm* yr^{-1} * m^{-1}), we could detect around the 70% (TPR) of the buildings belonging to classes 5 and 6, having the FNR of around 30%. Considering all the limitations related to the test-sample characterization, and that we did not consider the vulnerability variables related with the building characteristics, we believe this result represents a satisfactory outcome. However, there is still room for improvement.

In this sense, a possible improvement to overcome the geometric limitations of PSI (Section 3), would be using both ascending and descending data. Figure 10 shows a test we carried out in the case of Punta de la Mona Promontory, which includes the resorts of Punta de La Mona (hereafter La Mona), located in the western part, and Marina del Este (hereafter Marina), located in the eastern part. From the ascending acquisition geometry, La Mona is less "visible" than Marina (and vice-versa from descending geometry). A lower visibility means that we can measure a lower percentage of the real movement, with a lower resolution and thus higher noise over the signal. This is clearly reflected in the ADAs-QI (Figure 10 A and B). The main consequences are the underestimation of the velocity, and a lower sensitivity to the spatial variations of the movement. Here we test the methodology by integrating both the descending (Figure 10 A, C, E) and ascending results (Figure 10 B, D, F), without applying the horizontal-vertical (h-v) decomposition (Section 3). In Figure 10, the first row shows the displacement maps and the Enhanced ADAs, the second row shows the derived Gradient Intensity Maps, and the third row shows the Potential Damage Maps. The damage inventory map (Figure 10 G) and the final potential damage map (Figure 10 H) are shown at the bottom. For the final potential damage map, each building was assigned the maximum intensity value resulting from the two acquisition geometries. The orange rectangle (Figure 10 A and B) shows an area where measurement points are only obtained in descending geometry, preventing the application of h-v decomposition. Despite this limitation, our methodology allowed to detect the strongest displacement intensity gradient derived from the descending orbit PSI displacement dataset. In any case, a possible way forward in our approach allows to systematically integrate the use of ascending and descending PSI displacement measurements.

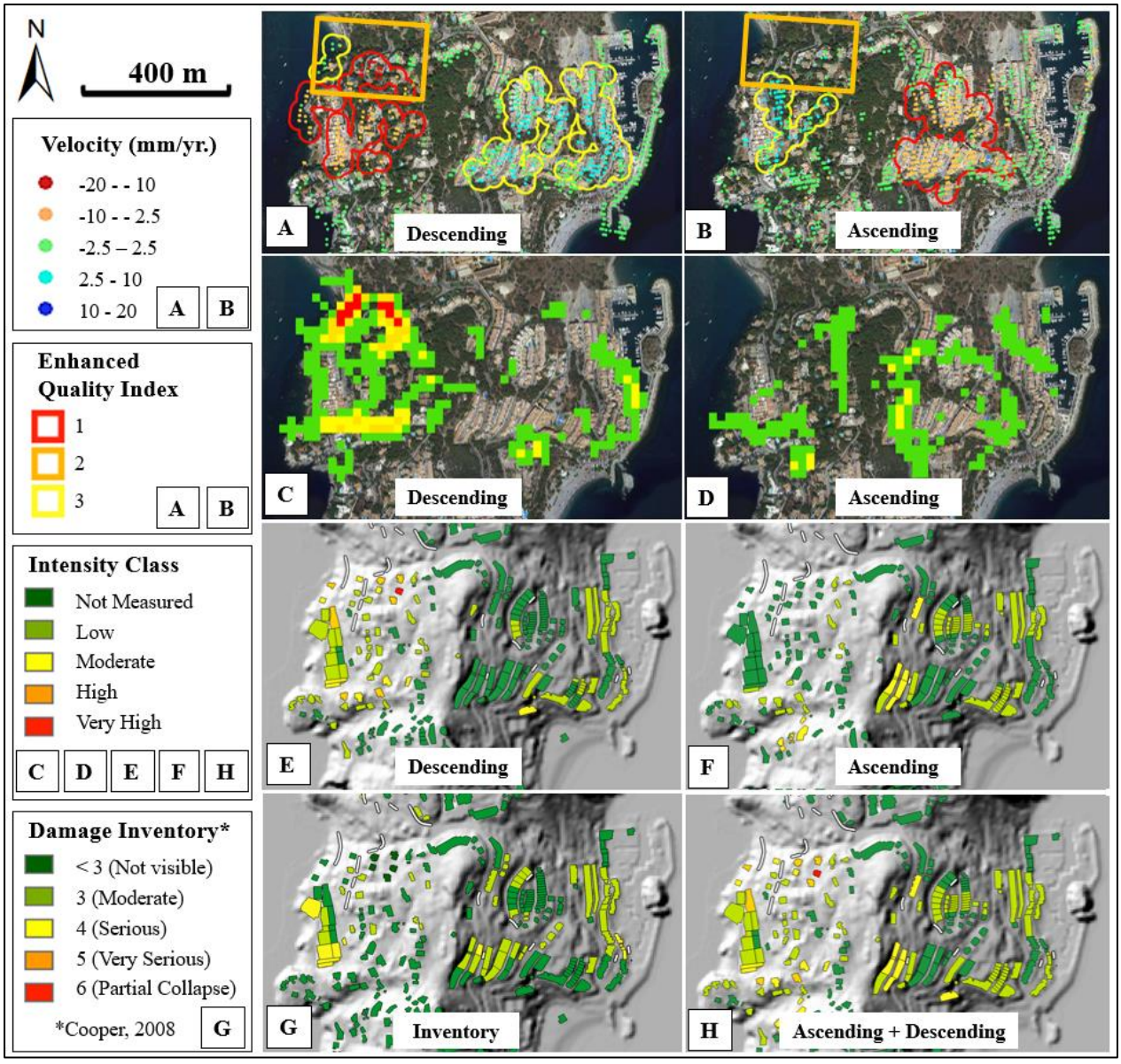

Figure 10 Combined use of ascending and descending data over the area of Punta de la Mona Promontory. A and B show the PSI velocity maps obtained by processing the selected descending and ascending datasets, respectively, toghether with their respective extracted ADAs. The second row shows the Gradient Intensity Maps derived from the descending (C) and ascending (D) velocity maps; E and F show respectively the Potential Damage Maps derived from the descending and ascending Gradient Intensity Maps. G and H show respectively the damage inventory map, and the final Potential Damage Map, obtained by combining both the ascending and descending results.

8 Conclusions

This work proposes a semi-automatic procedure to extract highly valuable information to identify damage prone buildings in urban environments from wide-area PSI displacement maps. The procedure starts by automatically identifying the most significant displacement clusters by using an improved version of the Active Deformation Areas (ADAs) approach. In the next step, the displacement intensity gradients are calculated over the selected ADAs, which are then classified into five levels of damage. This allows identifying the most critical zones in any urban environment before considering the presence, or absence, of exposed elements. The combination of the obtained displacement intensity gradients, with a map of exposed buildings, results into the Potential Damage Map, which allows performing a preliminary, fast classification of exposed buildings at risk. This map can be used as a base map for a more detailed building-based vulnerability and risk evaluation. To support the analysis of singular buildings and urban structures, our procedure also estimates the vectors of the displacement velocity gradients and the time series of the displacement intensity gradients.

The methodology was tested over a coastal area of the province of Granada (Spain), focusing on several resorts considerably affected by slope movements. This allowed to derive 175 ADAs from about 200,000 MPs. The 15 % of the resulting area was found to correspond to high or very high gradient intensity class, and 192 out of 633 buildings were identified to be prone to moderate or higher potential damage. These results demonstrate that the proposed methodology represents a cost-effective approach to preliminarily assess potential risk in urban environments in a semi-automatic way, providing a starting point for performing further analyses and investigations at a more detailed scale in specific locations (such as the analysis of singular buildings). The procedure, which exploits open, free and worldwide available remote sensing data (e.g. Sentinel-1, SRTM, and OpenStreetMap), is designed in light of the new European Ground Motion Service (EGMS) and its pan-European free-for-all PSI displacement map, which will soon be available. If automatized, it could be tested and improved using the different product levels provided by the

EGMS, i.e., using as input both the ascending and descending PSI maps (full resolution), and the horizontal and vertical maps derived from them (reduced resolution).

To refine the presented approach, several aspects could be improved. These include the selection of more significant thresholds or the adoption of a method to assess the reliability of each estimation, although both tasks would require longer monitoring periods. Moreover, a future study for an improved product will be the inclusion of supplementary information among the input data of the methodology, although this would be subjected to (site-specific) limitations related to data availability. Such information could include local geology, building and foundation typology, or building construction year. These improvements could have a positive impact on the performance of the methodology, leading to the generation of much more accurate results. Such results would be of high interest for different actors involved in urban planning and landscape management, including public institutions, architects, civil engineers, insurance companies, etc. In this sense, a possible application of the described method approach, might be the evaluation of real estate for purchase and sale, an area where unstable ground generates great economic losses, also causing serious legal problems for both the public and private sectors (as occurred in the study area). Thus, the development of InSAR post-processing tools such as the one provided in this work, could allow avoiding future court proceedings and economic losses related to unstable ground.

9 Acknowledgements

This work was mainly supported by the European Regional Development Fund (ERDF) through the project "RISKCOAST" (SOE3/P4/E0868) of the Interreg SUDOE Programme. The work of C.R-C., J.P.G., J.M.A. was supported by the following funds: the "Ramón y Cajal" Programme (RYC-2017-23335) of the Spanish Ministry of Science; the project "MORPHOMED" (PID2019-107138RB-I00) funded by MCIN / SRA (State Research Agency / 10.13039/501100011033); and FEDER/Junta de Andalucía-Consejería de Transformación Económica, Industria, Conocimiento y Universidades/Projects (B-RNM-305-UGR18, A-RNM-508-UGR20 and P18-RT-3632).

10 References

Antronico, L., Borrelli, L., Coscarelli, R., Gullà, G., 2015. Time evolution of landslide damages to buildings: the case study of Lungro (Calabria, southern Italy). Bulletin of Engineering Geology and the Environment 74, 47–59. https://doi.org/10.1007/s10064-014-0591-y

Azañón, J.M., Garcia-Dueñas, V., Martinez-Martinez, J.M., Crespo-Blanc, A., 1994. Alpujarride tectonic sheets in the central Betics and similar eastern allochthonous units (SE Spain). Comptes rendus de l'Académie des sciences. Série 2. Sci de la terre et des planètes 318, 667–674.

Barra, A., Monserrat, O., Mazzanti, P., Esposito, C., Crosetto, M., Scarascia Mugnozza, G., 2016. First insights on the potential of Sentinel-1 for landslides detection. Geomatics, Natural Hazards and Risk 7. https://doi.org/10.1080/19475705.2016.1171258

Barra, A., Monserrat, O., Solari, L., Herrera, G., Lopez, C., Onori, R., Reichenbach, P., González-Alonso, E., Mateos, R.M., Bianchini, S., Crosetto, M., 2018. The safety project: Sentinel-1 for the management of geological risk, in: WIT Transactions on Engineering Sciences. https://doi.org/10.2495/RISK180221

Barra, A., Solari, L., Béjar-Pizarro, M., Monserrat, O., Bianchini, S., Herrera, G., Crosetto, M., Sarro, R., González-Alonso, E., Mateos, R.M., Ligüerzana, S., López, C., Moretti, S., 2017. A methodology to detect and update active deformation areas based on Sentinel-1 SAR images. Remote Sensing 9, 1002. https://doi.org/10.3390/rs9101002

Béjar-Pizarro, M., Notti, D., Mateos, R.M., Ezquerro, P., Centolanza, G., Herrera, G., Bru, G., Sanabria, M., Solari, L., Duro, J., Fernández, J., 2017. Mapping vulnerable urban areas affected by slow-moving landslides using Sentinel-1InSAR data. Remote Sensing 9. https://doi.org/10.3390/rs9090876

Bianchini, S., Cigna, F., Righini, G., Proietti, C., Casagli, N., 2012. Landslide HotSpot Mapping by means of Persistent Scatterer Interferometry. Environmental Earth Sciences 67, 1155–1172. https://doi.org/10.1007/S12665-012-1559-5/FIGURES/8

Bianchini, S., Pratesi, F., Nolesini, T., Casagli, N., 2015. Building Deformation Assessment by Means of Persistent Scatterer Interferometry Analysis on a Landslide-Affected Area: The Volterra (Italy) Case Study. Remote Sensing 2015, Vol. 7, Pages 4678-4701 7, 4678–4701. https://doi.org/10.3390/RS70404678

Bonì, R., Pilla, G., Meisina, C., 2016. Methodology for detection and interpretation of ground motion areas with the A-DinSAR time series analysis. Remote Sensing 8. https://doi.org/10.3390/rs8080686

Boscawen Burland, J., Wroth, C.P., 1975. Settlement of Buildings and Associated Damage. No. CP 33/75.

Botey i Bassols, J., Vàzquez-Suñé, E., Crosetto, M., Barra, A., Gerard, P., 2021. D-InSAR monitoring of ground deformation related to the dewatering of construction sites. A case study of Glòries Square, Barcelona. Engineering Geology 286. https://doi.org/10.1016/j.enggeo.2021.106041

Bovenga, F., Pasquariello, G., Refice, A., 2021. Statistically-based trend analysis of mtinsar displacement time series. Remote Sensing 13. https://doi.org/10.3390/RS13122302

Burrough, P.A., Mcdonnell, R.A., 1998. Principles of Geographical Information Systems. Oxford University Press, New York.

Calò, F., Ardizzone, F., Castaldo, R., Lollino, P., Tizzani, P., Guzzetti, F., Lanari, R., Angeli, M.G., Pontoni, F., Manunta, M., 2014. Enhanced landslide investigations through advanced DInSAR techniques: The Ivancich case study, Assisi, Italy. Remote Sensing of Environment 142, 69–82. https://doi.org/10.1016/J.RSE.2013.11.003

Cascini, L., Bonnard, C., Corominas, J., Jibson, R., Montero-Olarte, J., 2005. Landslide hazard and risk zoning for urban planning and development. Landslide risk management. CRC Press. 209–2046.

780 Cascini, L., Peduto, D., Pisciotta, G., Arena, L., Ferlisi, S., Fornaro, G., 2013. The combination of DInSAR
781 and facility damage data for the updating of slow-moving landslide inventory maps at medium scale.
782 Natural Hazards and Earth System Sciences 13, 1527–1549. https://doi.org/10.5194/nhess-13-1527-
783 2013

784 Chacón, J., Alameda-Hernández, P., Chacón, E., Delgado, J., el Hamdouni, R., Fernández, P., Fernández,
785 T., Gómez-López, J.M., Irigaray, C., Jiménez-Perálvarez, J., Llopis, L., Moya, J., Olóriz, F.,
786 Palenzuela, J.A., 2019. The Calaiza landslide on the coast of Granada (Andalusia, Spain). Bulletin of
787 Engineering Geology and the Environment 78, 2107–2124. https://doi.org/10.1007/s10064-018-1246-
788 1

789 Chacón, J., el Hamdouni, R., Irigaray, C., Jiménez Perálvarez, J., Fernández, P., Fernández, T., Alameda,
790 P., Palenzuela, J.A., Moya, J., 2016. Landslides in the Coast of Almuñécar and its surround. Geogaceta
791 59, 87–90.

792 Chacón, J., Irigaray, C., del Castillo, T.F., el Hamdouni, R., Jiménez-Perálvarez, J., Alameda, P., Moya, J.,
793 Palenzuela, J.A., 2014. Urban landslides at the south of Sierra Nevada and coastal areas of the Granada
794 province (Spain). Landslide Science for a Safer Geoenvironment 3, 425–430.
795 https://doi.org/10.1007/978-3-319-04996-0_65

796 Chacón, J., Irigaray, C., Fernández, T., 2007. Los movimientos de ladera de la Provincia de Granada, in:
797 Atlas de Riesgos Naturales. Diputación de Granada–Instituto Geológico y Minera de España, Madrid.

798 Cigna, F., Cabral-Cano, E., Osmanoglu, B., Dixon, T.H., Wdowinski, S., 2011. Detecting subsidence-
799 induced faulting in Mexican urban areas by means of persistent scatterer interferometry and subsidence
800 horizontal gradient mapping. International Geoscience and Remote Sensing Symposium (IGARSS)
801 2125–2128. https://doi.org/10.1109/IGARSS.2011.6049585

Cigna, F., Tapete, D., 2021. Present-day land subsidence rates, surface faulting hazard and risk in Mexico City with 2014–2020 Sentinel-1 IW InSAR. Remote Sensing of Environment 253. https://doi.org/10.1016/j.rse.2020.112161

Confuorto, P., del Soldato, M., Solari, L., Festa, D., Bianchini, S., Raspini, F., Casagli, N., 2021. Sentinel-1-based monitoring services at regional scale in Italy: State of the art and main findings. International Journal of Applied Earth Observation and Geoinformation 102, 102448. https://doi.org/10.1016/J.JAG.2021.102448

Cooper, A.H., 2008. The classification, recording, databasing and use of information about building damage due to subsidence and landslides. Quarterly Journal of Engineering Geology and Hydrogeology 41. https://doi.org/10.1144/1470-9236/07-223

Costantini, M., Minati, F., Trillo, F., Ferretti, A., Novali, F., Passera, E., Dehls, J., Larsen, Y., Marinkovic, P., Eineder, M., Brcic, R., Siegmund, R., Kotzerke, P., Probeck, M., Kenyeres, A., Proietti, S., Solari, L., Andersen, H.S., 2021. European Ground Motion Service (EGMS), in: IEEE (Ed.), 2021 IEEE International Geoscience and Remote Sensing Symposium IGARSS. Institute of Electrical and Electronics Engineers (IEEE), Brussels, Belgium, pp. 3293–3296. https://doi.org/10.1109/IGARSS47720.2021.9553562

Crosetto, M., Monserrat, O., Cuevas-González, M., Devanthéry, N., Crippa, B., 2016a. Persistent Scatterer Interferometry: A review. ISPRS Journal of Photogrammetry and Remote Sensing 115, 78–89. https://doi.org/10.1016/J.ISPRSJPRS.2015.10.011

Crosetto, M., Monserrat, O., Devanthéry, N., Cuevas-González, M., Barra, A., Crippa, B., 2016b. Persistent scatterer interferometry using Sentinel-1 data, in: International Archives of the Photogrammetry, Remote Sensing and Spatial Information Sciences - ISPRS Archives. https://doi.org/10.5194/isprsarchives-XLI-B7-835-2016

Crosetto, M., Solari, L., Balasis-Levinsen, J., Bateson, L., Casagli, N., Frei, M., Oyen, A., Moldestad, D.A., Mróz, M., 2021. Deformation monitoring at european scale: The copernicus ground motion service. International Archives of the Photogrammetry, Remote Sensing and Spatial Information Sciences - ISPRS Archives 43, 141–146. https://doi.org/10.5194/ISPRS-ARCHIVES-XLIII-B3-2021-141-2021

Crosetto, M., Solari, L., Balasis-Levinsen, J., Casagli, N., Frei, M., Oyen, A., Moldestad, D.A., 2020a. Ground deformation monitoring at continental scale: The european ground motion service. International Archives of the Photogrammetry, Remote Sensing and Spatial Information Sciences - ISPRS Archives 43, 293–298. https://doi.org/10.5194/ISPRS-ARCHIVES-XLIII-B3-2020-293-2020

Crosetto, M., Solari, L., Mróz, M., Balasis-Levinsen, J., Casagli, N., Frei, M., Oyen, A., Moldestad, D.A., Bateson, L., Guerrieri, L., Comerci, V., Andersen, H.S., 2020b. The evolution of wide-area DInSAR: From regional and national services to the European ground motion service. Remote Sensing 12, 2043. https://doi.org/10.3390/RS12122043

Dehls, J.F., Larsen, Y., Marinkovic, P., Lauknes, T.R., Stodle, D., Moldestad, D.A., 2019. INSAR.No: A National Insar Deformation Mapping/Monitoring Service in Norway - From Concept to Operations. International Geoscience and Remote Sensing Symposium (IGARSS) 5461–5464. https://doi.org/10.1109/IGARSS.2019.8898614

del Soldato, M., Solari, L., Poggi, F., Raspini, F., Tomás, R., Fanti, R., Casagli, N., 2019. Landslide-induced damage probability estimation coupling InSAR and field survey data by fragility curves. Remote Sensing 11. https://doi.org/10.3390/RS11121486

Devanthéry, N., Crosetto, M., Monserrat, O., Crippa, B., Mróz, M., 2019. Data analysis tools for persistent scatterer interferometry based on Sentinel-1 data. European Journal of Remote Sensing 52, 15–25. https://doi.org/10.1080/22797254.2018.1554981

847 Devanthéry, N., Crosetto, M., Monserrat, O., Cuevas-González, M., Crippa, B., 2014. An Approach to
848 Persistent Scatterer Interferometry. Remote Sensing 2014, Vol. 6, Pages 6662-6679 6, 6662–6679.
849 https://doi.org/10.3390/RS6076662

850 Drougkas, A., Verstrynge, E., van Balen, K., Shimoni, M., Croonenborghs, T., Hayen, R., Declercq, P.Y.,
851 2020. Country-scale InSAR monitoring for settlement and uplift damage calculation in architectural
852 heritage structures: Structural Health Monitoring 1–20. https://doi.org/10.1177/1475921720942120

853 Ezquerro, P., del Soldato, M., Solari, L., Tomás, R., Raspini, F., Ceccatelli, M., Fernández-Merodo, J.A.,
854 Casagli, N., Herrera, G., 2020. Vulnerability assessment of buildings due to land subsidence using
855 insar data in the ancient historical city of pistoia (Italy). Sensors (Switzerland) 20.
856 https://doi.org/10.3390/s20102749

857 Farr, T.G., Rosen, P.A., Caro, E., Crippen, R., Duren, R., Hensley, S., Kobrick, M., Paller, M., Rodriguez,
858 E., Roth, L., Seal, D., Shaffer, S., Shimada, J., Umland, J., Werner, M., Oskin, M., Burbank, D.,
859 Alsdorf, D.E., 2007. The Shuttle Radar Topography Mission. Reviews of Geophysics 45, 2004.
860 https://doi.org/10.1029/2005RG000183

861 Fell, R., Corominas, J., Bonnard, C., Cascini, L., Leroi, E., Savage, W.Z., 2008. Guidelines for landslide
862 susceptibility, hazard and risk zoning for land-use planning on behalf of the JTC-1 Joint Technical
863 Committee on Landslides and Engineered Slopes. Engineering Geology 102, 99–111.
864 https://doi.org/10.1016/j.enggeo.2008.03.014

865 Ferlisi, S., Gullà, G., Nicodemo, G., Peduto, D., 2019. A multi-scale methodological approach for slow-
866 moving landslide risk mitigation in urban areas, southern Italy. Euro-Mediterranean Journal for
867 Environmental Integration 4, 1–15. https://doi.org/10.1007/S41207-019-0110-4

868 Ferretti, A., Prati, C., Rocca, F., 2001. Permanent scatterers in SAR interferometry. IEEE Transactions on
869 Geoscience and Remote Sensing 39, 8–20. https://doi.org/10.1109/36.898661

Hanssen, R.F., 2001. Radar interferometry : data interpretation and error analysis, Springer Science & Business Media.

Kalia, A.C., 2017. User driven products in the context of the ground motion service Germany. International Geoscience and Remote Sensing Symposium (IGARSS) 2017-July, 1688–1691. https://doi.org/10.1109/IGARSS.2017.8127299

Kalia, A.C., Frei, M., Lege, T., 2017. A Copernicus downstream-service for the nationwide monitoring of surface displacements in Germany. Remote Sensing of Environment 202, 234–249. https://doi.org/10.1016/J.RSE.2017.05.015

Krishnakumar, V., Qiu, Z., Monserrat, O., Barra, A., López-Vinielles, J., Reyes-Carmona, C., Gao, Q., Cuevas-González, M., Palamà, R., Crippa, B., Gili, J.A., 2021. Sentinel-1 a-dinsar approaches to map and monitor ground displacements. Remote Sensing 13. https://doi.org/10.3390/rs13061120

Lancellotta, Renato., 2004. Geotecnica. Zanichelli.

López-Vinielles, J., Ezquerro, P., Fernández-Merodo, J.A., Béjar-Pizarro, M., Monserrat, O., Barra, A., Blanco, P., García-Robles, J., Filatov, A., García-Davalillo, J.C., Sarro, R., Mulas, J., Mateos, R.M., Azañón, J.M., Galve, J.P., Herrera, G., 2020. Remote analysis of an open-pit slope failure: Las Cruces case study, Spain. Landslides 17, 2173–2188. https://doi.org/10.1007/s10346-020-01413-7

Mansour, M.F., Morgenstern, N.R., Martin, C.D., 2011. Expected damage from displacement of slow-moving slides. Landslides 8, 117–131. https://doi.org/10.1007/S10346-010-0227-7/FIGURES/6

Massonnet, D., Briole, P., Arnaud, A., 1995. Deflation of Mount Etna monitored by spaceborne radar interferometry. Nature 1995 375:6532 375, 567–570. https://doi.org/10.1038/375567a0

Massonnet, D., Feigl, K.L., 1998. RADAR INTERFEROMETRY AND ITS APPLICATION TO CHANGES IN THE EARTH'S SURFACE. https://doi.org/10.1029/97RG03139

892 Massonnet, D., Rossi, M., Carmona, C., Adragna, F., Peltzer, G., Feigl, K., Rabaute, T., 1993. The
893 displacement field of the Landers earthquake mapped by radar interferometry. Nature 1993 364:6433
894 364, 138–142. https://doi.org/10.1038/364138A0

895 Mateos, R.M., Ezquerro, P., Luque-Espinar, J.A., Béjar-Pizarro, M., Notti, D., Azañón, J.M., Montserrat,
896 O., Herrera, G., Fernández-Chacón, F., Peinado, T., Galve, J.P., Pérez-Peña, V., Fernández-Merodo,
897 J.A., Jiménez, J., 2017. Multiband PSInSAR and long-period monitoring of land subsidence in a
898 strategic detrital aquifer (Vega de Granada, SE Spain): An approach to support management decisions.
899 Journal of Hydrology 553, 71–87. https://doi.org/10.1016/j.jhydrol.2017.07.056

900 Mateos, R.M., López-Vinielles, J., Poyiadji, E., Tsagkas, D., Sheehy, M., Hadjicharalambous, K., Liscák,
901 P., Podolski, L., Laskowicz, I., Iadanza, C., Gauert, C., Todorović, S., Auflič, M.J., Maftei, R.,
902 Hermanns, R.L., Kociu, A., Sandić, C., Mauter, R., Sarro, R., Béjar, M., Herrera, G., 2020. Integration
903 of landslide hazard into urban planning across Europe. Landscape and urban planning 196.
904 https://doi.org/10.1016/j.landurbplan.2019.103740

905 Mavrouli, O., Fotopoulou, S., Pitilakis, K., Zuccaro, G., Corominas, J., Santo, A., Cacace, F., de Gregorio,
906 D., di Crescenzo, G., Foerster, E., Ulrich, T., 2014. Vulnerability assessment for reinforced concrete
907 buildings exposed to landslides. Bulletin of Engineering Geology and the Environment 73, 265–289.
908 https://doi.org/10.1007/S10064-014-0573-0/FIGURES/23

909 Measor, E.O., Cooling, L.F., Souza, R.W., Golder, H.Q., Williams, G.M.J., Cassel, F.L., Flint, A.R.,
910 Meyerhof, G.G., Terzaghi, K., Ripley, C.F., Peck, R.B., Deere, D.U., Capacete, J.L., Schriever, W.R.,
911 Plewes, W.G., Ward, W.H., Skempton, A.W., 1956. DISCUSSION. THE ALLOWABLE
912 SETTLEMENTS OF BUILDINGS. Proceedings of the Institution of Civil Engineers 5, 768–784.
913 https://doi.org/https://doi.org/10.1680/ipeds.1956.12204

914 Meisina, C., Zucca, F., Notti, D., Colombo, A., Cucchi, A., Savio, G., Giannico, C., Bianchi, M., 2008.
915 Geological Interpretation of PSInSAR Data at Regional Scale. Sensors 2008, Vol. 8, Pages 7469-7492
916 8, 7469–7492. https://doi.org/10.3390/S8117469

917 Mirmazloumi, S.M., Wassie, Y., Navarro, A., Palamà, R., Krishnakumar, V., Barra, A., Cuevas-González,
918 M., Crosetto, M., Monserrat, O., 2022. Classification of ground deformation using sentinel-1 persistent
919 scatterer interferometry time series. GIScience & Remote Sensing 59, 374–392.
920 https://doi.org/10.1080/15481603.2022.2030535

921 Monserrat, O., Barra, A., Herrera, G., Bianchini, S., Lopez, C., Onori, R., Reichenbach, P., Sarro, R.,
922 Mateos, R.M., Solari, L., Ligüérzana, S., Carralero, I.P., 2018. SAFETY project: Sentinel-1 based
923 tools for geohazards monitoring and management, in: International Archives of the Photogrammetry,
924 Remote Sensing and Spatial Information Sciences - ISPRS Archives. https://doi.org/10.5194/isprs-
925 archives-XLII-3-W4-351-2018

926 Montalti, R., Solari, L., Bianchini, S., del Soldato, M., Raspini, F., Casagli, N., 2019. A Sentinel-1-based
927 clustering analysis for geo-hazards mitigation at regional scale: a case study in Central Italy.
928 Geomatics, Natural Hazards and Risk 10, 2257–2275.
929 https://doi.org/10.1080/19475705.2019.1690058

930 Navarro, J.A., Cuevas, M., Tomás, R., Barra, A., Crosetto, M., 2019. A toolset to detect and classify active
931 deformation areas using interferometric SAR data, in: GISTAM 2019 - Proceedings of the 5th
932 International Conference on Geographical Information Systems Theory, Applications and
933 Management. https://doi.org/10.5220/0007617701670174

934 Navarro, J.A., Tomás, R., Barra, A., Pagán, J.I., Reyes-Carmona, C., Solari, L., Vinielles, J.L., Falco, S.,
935 Crosetto, M., 2020. ADAtools: Automatic detection and classification of active deformation areas
936 from PSI displacement maps. ISPRS International Journal of Geo-Information 9.
937 https://doi.org/10.3390/IJGI9100584

Notti, D., Galve, J.P., Mateos, R.M., Monserrat, O., Lamas-Fernández, F., Fernández-Chacón, F., Roldán-García, F.J., Pérez-Peña, J.V., Crosetto, M., Azañón, J.M., 2015. Human-induced coastal landslide reactivation. Monitoring by PSInSAR techniques and urban damage survey (SE Spain). Landslides 12, 1007–1014. https://doi.org/10.1007/s10346-015-0612-3

Notti, D., Herrera, G., Bianchini, S., Meisina, C., García-Davalillo, J.C., Zucca, F., 2014. A methodology for improving landslide PSI data analysis. International Journal of Remote Sensing 35, 2186–2214. https://doi.org/10.1080/01431161.2014.889864

Notti, D., Mateos, R.M., Monserrat, O., Devanthéry, N., Peinado, T., Roldán, F.J., Fernández-Chacón, F., Galve, J.P., Lamas, F., Azañón, J.M., 2016. Lithological control of land subsidence induced by groundwater withdrawal in new urban AREAS (Granada Basin, SE Spain). Multiband DInSAR monitoring. Hydrological Processes 30, 2317–2331. https://doi.org/10.1002/hyp.10793

Papoutsis, I., Kontoes, C., Alatza, S., Apostolakis, A., Loupasakis, C., 2020. InSAR greece with parallelized persistent scatterer interferometry: A national ground motion service for big copernicus sentinel-1 data. Remote Sensing 12, 1–27. https://doi.org/10.3390/RS12193207

Pastonchi, L., Barra, A., Monserrat, O., Luzi, G., Solari, L., Tofani, V., 2018. Satellite data to improve the knowledge of geohazards in World Heritage Sites. Remote Sensing 10. https://doi.org/10.3390/rs10070992

Pavić, G., Bulajić, B., Hadzima-Nyarko, M., 2019. The vulnerability of buildings from the osijek database. Frontiers in Built Environment 5, 66. https://doi.org/10.3389/FBUIL.2019.00066/BIBTEX

Peduto, D., Ferlisi, S., Nicodemo, G., Reale, D., Pisciotta, G., Gullà, G., 2017a. Empirical fragility and vulnerability curves for buildings exposed to slow-moving landslides at medium and large scales. Landslides 14, 1993–2007. https://doi.org/10.1007/s10346-017-0826-7

960 Peduto, D., Nicodemo, G., Cuevas-Gonzáles, M., Crosetto, M., 2019. Analysis of Damage to Buildings in
961 Urban Centers on Unstable Slopes via TerraSAR-X PSI Data: The Case Study of El Papiol Town
962 (Spain). IEEE Geoscience and Remote Sensing Letters 16, 1706–1710.
963 https://doi.org/10.1109/LGRS.2019.2907557

964 Peduto, D., Nicodemo, G., Maccabiani, J., Ferlisi, S., 2017b. Multi-scale analysis of settlement-induced
965 building damage using damage surveys and DInSAR data: A case study in The Netherlands.
966 Engineering Geology 218, 117–133. https://doi.org/10.1016/j.enggeo.2016.12.018

967 Polshin, D.E., Tokar, R.A., 1957. Maximum allowable non-uniform settlement of structures. 4th Int Conf
968 on Soil Mech and Found Eng 402.

969 Raspini, F., Bianchini, S., Ciampalini, A., del Soldato, M., Solari, L., Novali, F., del Conte, S., Rucci, A.,
970 Ferretti, A., Casagli, N., 2018. Continuous, semi-automatic monitoring of ground deformation using
971 Sentinel-1 satellites. Scientific Reports 8, 1–11. https://doi.org/10.1038/s41598-018-25369-w

972 Reyes-Carmona, C., Barra, A., Galve, J.P., Monserrat, O., Pérez-Peña, J.V., Mateos, R.M., Notti, D., Ruano,
973 P., Millares, A., López-Vinielles, J., Azañón, J.M., 2020. Sentinel-1 DInSAR for monitoring active
974 landslides in critical infrastructures: The case of the rules reservoir (Southern Spain). Remote Sensing
975 12. https://doi.org/10.3390/RS12050809

976 Salvi, S., Stramondo, S., Funning, G.J., Ferretti, A., Sarti, F., Mouratidis, A., 2012. The Sentinel-1 mission
977 for the improvement of the scientific understanding and the operational monitoring of the seismic
978 cycle. Remote Sensing of Environment 120, 164–174. https://doi.org/10.1016/j.rse.2011.09.029

979 Simancas, J.F., Campos, J., 1993. Compresión NNW-SSE tardi a postmetamórfica y extensión subordinada
980 en el Complejo Alpujárride (Dominio de Alborán, Orógeno Bético). Revista de la Sociedad Geológica
981 de España 6, 23–35.

Skempton, A.W., Macdonald, D.H., 1956. THE ALLOWABLE SETTLEMENTS OF BUILDINGS. Proceedings of the Institution of Civil Engineers 5, 727–768. https://doi.org/https://doi.org/10.1680/ipeds.1956.12202

Solari, L., Barra, A., Herrera, G., Bianchini, S., Monserrat, O., Béjar-Pizarro, M., Crosetto, M., Sarro, R., Moretti, S., 2018. Fast detection of ground motions on vulnerable elements using sentinel-1 InSAR data. Geomatics, Natural Hazards and Risk 9. https://doi.org/10.1080/19475705.2017.1413013

Solari, L., Bianchini, S., Franceschini, R., Barra, A., Monserrat, O., Thuegaz, P., Bertolo, D., Crosetto, M., Catani, F., 2020a. Satellite interferometric data for landslide intensity evaluation in mountainous regions. International Journal of Applied Earth Observation and Geoinformation 87. https://doi.org/10.1016/J.JAG.2019.102028

Solari, L., Montalti, R., Barra, A., Monserrat, O., Bianchini, S., Crosetto, M., 2020b. Multi-temporal satellite interferometry for fast-motion detection: An application to salt solution mining. Remote Sensing 12, 1–21. https://doi.org/10.3390/RS12233919

Tinti, S., Tonini, R., Bressan, L., Armigliato, A., Gardi, A., Guillande, R., Valencia, N., Scheer, S., 2011. Handbook of tsunami hazard and damage scenarios. JRC Scientific and Technical Reports 1–41. https://doi.org/10.2788/21259

Tomás, R., Pagán, J.I., Navarro, J.A., Cano, M., Pastor, J.L., Riquelme, A., Cuevas-González, M., Crosetto, M., Barra, A., Monserrat, O., Lopez-Sanchez, J.M., Ramón, A., Ivorra, S., del Soldato, M., Solari, L., Bianchini, S., Raspini, F., Novali, F., Ferretti, A., Costantini, M., Trillo, F., Herrera, G., Casagli, N., 2019. Semi-automatic identification and pre-screening of geological-geotechnical deformational processes using persistent scatterer interferometry datasets. Remote Sensing 11. https://doi.org/10.3390/rs11141675